

## Monte Carlo modeling of Io's [OI] 6300 Å and [SII] 6716 Å auroral emission in eclipse

C. Moore<sup>a,\*</sup>, K. Miki<sup>a</sup>, D.B. Goldstein<sup>a</sup>, K. Stapelfeldt<sup>a,b</sup>, P.L. Varghese<sup>a</sup>, L.M. Trafton<sup>a</sup>, R.W. Evans<sup>a,b</sup>

<sup>a</sup> The University of Texas at Austin, Austin, TX 78712, USA

<sup>b</sup> JPL, Caltech, USA

### ARTICLE INFO

#### Article history:

Received 28 July 2009

Revised 2 January 2010

Accepted 3 January 2010

Available online 22 January 2010

#### Keywords:

Io

Aurorae

Jupiter, Satellites

Satellites, Atmospheres

Collisional physics

### ABSTRACT

We present a Monte Carlo (MC) model of [OI] 6300 Å and [SII] 6716 Å emission from Io entering eclipse. The simulation accounts for the 3-D distribution of SO<sub>2</sub>, O, SO, S, and O<sub>2</sub> in Io's atmosphere, several volcanic plumes, and the magnetic field around Io. Thermal electrons from the jovian plasma torus are input along the simulation domain boundaries and move along the magnetic field lines distorted by Io, occasionally participating in collisions with neutrals. We find that the atmospheric asymmetry resulting from varying degrees of atmospheric collapse across Io (due to eclipse ingress) and the presence of volcanoes contributes significantly to the unique morphology of the [OI] 6300 Å emission. The [OI] radiation lifetime of ~134 s limits the emission to regions that have a sufficiently low neutral density so that intermolecular collisions are rare. We find that at low altitudes (typically <40 km) and in volcanic plumes (Pele, Prometheus, etc.) the number density is large enough (>4 × 10<sup>9</sup> cm<sup>-3</sup>) to collisionally quench nearly all (>95%) of the excited oxygen for reasonable quenching efficiencies. Upstream (relative to the plasma flow), Io's perturbation of the jovian magnetic field mirrors electrons with high pitch angles, while downstream collisions can trap the electrons. This magnetic field perturbation is one of the main physical mechanisms that results in the upstream/downstream brightness asymmetry in [OI] emission seen in the observation by Trauger et al. (Trauger, J.T., Stapelfeldt, K.R., Ballester, G.E., Clarke, J.I., 1997. HST observations of [OI] emissions from Io in eclipse. AAS-DPS Abstract (1997DPS29.1802T)). There are two other main causes for the observed brightness asymmetry. First, the observation's viewing geometry of the wake spot crosses the dayside atmosphere and therefore the wake's observational field of view includes higher oxygen column density than the upstream side. Second, the phased entry into eclipse results in less atmospheric collapse and thus higher collisional quenching on the upstream side relative to the wake. We compute a location (both in altitude and latitude) for the intense wake emission feature that agrees reasonably well with this observation. Furthermore, the peak intensity of the simulated wake feature is less than that observed by a factor of ~3, most likely because our model does not include direct dissociation-excitation of SO<sub>2</sub> and SO. We find that the latitudinal location of the emission feature depends not so much on the tilt of the magnetic field as on the relative north/south flux tube depletion that occurs due to Io's changing magnetic latitude in the plasma torus. From 1-D simulations, we also find that the intensity of [SII] 6716 and 6731 Å emission is much weaker than that of [OI] even if the [SII] excitation cross section is 10<sup>3</sup> times larger than excitation to [OI]. This is because the density of S<sup>+</sup> is much less than that of O and because the Einstein-A coefficient of the [SII] emission is a factor of ~10 smaller than that of [OI].

© 2010 Elsevier Inc. All rights reserved.

## 1. Introduction

Io possesses a spectacular aurora concentrated at low latitudes that differs from Earth's polar aurora. While it is known that electrons (and, to a lesser extent, protons) traveling along the magnetic field lines result in a polar aurora near Earth, the precise mechanism that produces the ionian 6300 Å auroral features remains

\* Corresponding author. Address: Department of Aerospace Engineering and Engineering Mechanics, The University of Texas at Austin, 1 University Station, C6600, Austin, TX 78712, USA.

E-mail address: [moorech@ices.utexas.edu](mailto:moorech@ices.utexas.edu) (C. Moore).

uncertain. Several general features characterizing Io's aurora have been observed over the years: an equatorial band located along the extended jovian magnetic equatorial plane, a limb glow near each pole, a bright spot in the wake, and extended diffuse emission particularly on the downstream side. In May 1997, Trauger et al. (1997) observed Io with the Wide Field and Planetary Camera 2 (WFPC2) ~10 min after it entered Jupiter's shadow. Their observations showed several bright regions of [OI] 6300 Å emission (shown in Fig. 6), and virtually no [SII] 6716 and 6731 Å emission. Oliversen et al. (2001) showed that the disc-averaged [OI] 6300 Å intensity of Io varies with Io's system III longitude. Rutherford (2002) and Rutherford et al. (2003) noted that the brightness ratio

between the north and south limb glows agreed with the ratio of the thermal electron column densities in the plasma torus above the respective poles. Furthermore, the latitude (on Io) of the equatorial spots seems to be correlated with Io's system III longitude based on many images of the aurora at different system III longitudes (Roesler et al., 1999; Retherford et al., 2000; Geissler et al., 2001). A recent series of auroral observations during eclipse as Io crosses the torus by NASA's Cassini spacecraft definitively show that the equatorial auroral spots gradually shift in latitude (relative to Io) as Io's system III longitude changes (Porco et al., 2003; Geissler et al., 2004b).

The only significant excitation mechanism of the observed [OI] emission during eclipse comes from the interaction of the jovian plasma torus electrons (and ions) with Io's atmosphere. Therefore, the properties of the impinging electrons (and ions) strongly influence the auroral emissions seen in eclipse. Voyager 1 detected a ~6 MA current of high-energy electrons along the Io flux tube extending between Io and the jovian north and south poles (Acuña et al., 1981). We define a flux tube as the total column of plasma along a magnetic field line, therefore as the plasma convects with the magnetic field, so does the flux tube. The jovian plasma torus consists predominantly of O<sup>+</sup>, S<sup>+</sup> and thermal electrons that spiral along the rotating jovian magnetic field lines which rotate past Io at a relative speed of ~57 km/s. At Io's orbit, the thermal electrons in the plasma have a nominal number density of ~3600 m<sup>-3</sup> (Frank et al., 1996) and a temperature of ~5 eV (Sittler and Strobel, 1987).

Bhardwaj and Michael (1999b) used a 1-D Monte Carlo (MC) model to study the degradation of electrons in an SO<sub>2</sub> gas. The data generated by the MC model was then used in an analytical model to study the spatial degradation of energetic (10 keV) electrons and simulate the far ultraviolet (FUV) OI and SI emission (Bhardwaj and Michael, 1999a). Their model was able to examine the dependence of emission intensity on the initial electron energy, though the calculated intensities were more than two orders of magnitude less than the HST-observed intensities (Clarke et al., 1994). They demonstrated that electron energies greater than ~10 keV would not produce the emission profile observed because such electrons mostly hit the surface without interacting with the atmosphere. Michael and Bhardwaj (2000a,b) continued the previous 1-D work and found that field aligned lower energy electrons (0.1–5 keV) can explain the observed S and O FUV brightness.

Io perturbs the jovian magnetic field in its vicinity (Frank et al., 1996); furthermore, Kivelson et al. (2001) found that Io does not have a substantial intrinsic magnetic field. Combi et al. (1998) developed a global 3-D magnetohydrodynamic (MHD) simulation for mass-loaded flow that can explain the magnetic field measurements near Io without requiring an intrinsic ionian field; however, their method assumes perfect conductivity and an imposed ionization distribution. Their model could reproduce Frank et al.'s (1996) observation of the magnetic field disturbance near Io and obtain good qualitative matches to the plasma density peak and the plasma pressure in Io's wake. Saur et al. (1999, 2000) calculated the density, velocity and temperature of thermal electrons and one representative ion species, and the electric field in a self-consistent manner, but assumed a spherically symmetric atmosphere and a spatially uniform jovian magnetic field, requiring the actual perturbation in the magnetic field magnitude about Io to be relatively small. Their model was able to describe certain aspects of Io's FUV aurora, such as the relative brightness and position of the sub-jovian and anti-jovian spots. Specifically, they investigated the formation of [OI] 1356 Å equatorial spots at western elongation and found that the Hall effect causes the anti-jovian spot to be brighter than the sub-jovian spot. Saur et al. (2002) gave magnetic field predictions for a polar pass over Io and interpreted plasma torus observations from several Galileo flybys without the assumption that Io had an internal magnetic field. Their analysis also sug-

gested that Io's atmosphere is longitudinally asymmetric due to momentum transfer from the plasma as it flows around Io's atmosphere and that the Hall effect generates rotated Alfvén wings. Saur and Strobel (2004) examined Io's delayed electrodynamic response and [OI] 1356 Å emission during eclipse. By assuming the entire sublimation atmosphere is in equilibrium with the cooling surface during eclipse and considering an improved equatorial atmospheric model, they were able to constrain the volcanic contribution to the atmospheric column density to ~3–5 × 10<sup>14</sup> cm<sup>-2</sup>. More recently, Lipatov and Combi (2006) performed a hybrid simulation of the magnetic and electric environment about Io with fluid (MHD) electrons and kinetic ions. Through this approach, the magnetic and electric fields were solved self-consistently and provided good comparison to the Galileo IO flyby data.

Clearly, the structure of the ionian atmosphere is critical to calculations of the auroral emission. Io's SO<sub>2</sub> atmosphere is partially sustained by sublimation of non-uniform surface ice and therefore the sublimation atmosphere is concentrated near the frost-covered dayside equatorial regions of Io's surface. On the nightside of Io the SO<sub>2</sub> number density drops significantly since SO<sub>2</sub> is condensable at the nightside temperatures. Wong and Johnson (1996) examined the effect of condensable SO on the overall atmosphere. They found that, if SO were condensable, the SO<sub>2</sub> column density at the anti-solar point fell by a factor of ~10<sup>3</sup> relative to when SO was considered non-condensable. Austin and Goldstein (2000) used a 2-D DSMC simulation to model Io's rarefied atmosphere and found circumplanetary flow from the sub-solar point to the nightside develops and that a shock forms near the terminator. Furthermore, they found that the non-condensable species (SO and O<sub>2</sub> in their model) build up on the nightside. Wong and Smyth (2000) simulated Io's atmosphere out of eclipse using a steady, multi-species, 2-D continuum model. They found that due to the atmospheric flow from the sub-solar point to the nightside, non-condensables tend to accumulate and dominate the nightside atmosphere. Smyth and Wong (2004) also showed that the O density is enhanced at high altitudes through dissociation of SO<sub>2</sub>, O<sub>2</sub>, and SO by thermal electrons from the plasma torus. This higher O concentration at high altitude should result in diffuse, extended regions of radiative [OI] emission. Since the [OI] aurora observations are taken during eclipse, the sublimation atmosphere's response to the cooling surface will be important to the emission morphology. Moore et al. (2009) simulated the collapse of a column of SO<sub>2</sub> and non-condensable gas as the surface cooled. They found that the SO<sub>2</sub> density near the surface fell during the first ~20 min of eclipse while a quasi-steady diffusion layer of the non-condensable gas formed. Once the diffusion layer was several mean free paths thick, the collapse slowed substantially since the SO<sub>2</sub> had to diffuse through the layer to reach the surface and condense. They also found that the gas properties changed very little above ~20 km early in eclipse.

The aim of this paper is to simulate the interaction of electrons from the jovian plasma torus with Io's atmosphere, and thereby reproduce the specific auroral features (at [OI] 6300 Å and [SII] 6716 and 6731 Å) observed when Io enters eclipse while solar excitations do not occur. In our model, we do not calculate the magnetic and electric fields but specify them using data from a fixed boundary, mass loaded MHD simulation provided by Combi et al. (1998). The most recent simulated fields (Lipatov and Combi, 2006) have not yet been put into the model. In this sense, our model is not self-consistent with regard to the magnetic and electric fields; however, we consider several important factors that are neglected in other more simplified models of [OI] emission in the vicinity of Io. These include a non-uniform neutral atmosphere from sublimation of surface frosts and volcanic plumes, a simple model of the progressive collapse of the atmosphere across Io's surface during eclipse, accurate electron-neutral collision cross sections for 39 major reactions, and an approximate model of the

flux tube depletion as Io changes latitude in the plasma torus. We discuss the atmospheric and volcanic models in detail in Section 2, followed by a detailed description of our physical models for excitation and emission. In Section 3 we first present 1-D simulation results which investigate the lack of [SII] emission. Then we provide 3-D results examining the effects of the asymmetric sublimation neutral density atmosphere, volcanoes, perturbed magnetic field, and Io's latitudinal location in the plasma torus on [OI] 6300 Å emission. Finally, in Section 4, we summarize our results.

## 2. Physical model

The multiple interaction mechanisms between the jovian magnetosphere and Io's atmosphere make it difficult to simulate all the physical processes around Io in detail and obtain the various observed auroral features. In general, we would need to consider plasma dynamics in the entire torus, chemical reactions, photo-reactions, and unsteady gas dynamics to describe the atmospheric flow driven by the sublimation/condensation of  $\text{SO}_2$  frost and the episodic volcanoes.

### 2.1. Model overview

Our numerical approach focuses on the two most important physical mechanisms for auroral emissions around Io: (1) electron dynamics and (2) neutral dynamics. The electron dynamics are simulated using our “Excitation” routine, which follows electron motion along field lines and computes electron–neutral collisions. The neutral dynamics are modeled using our “Emission” routine to simulate the transport of excited neutrals as they de-excite via collisions with other neutrals or through spontaneous decay based on the Einstein-A coefficients for each emission process that produces emission ([OI] 6300 Å or [SII] 6716 Å). The simulation can be split into the two sequential routines (Excitation and Emission) because the electron-[OI] mean collisional de-excitation time is long ( $>\sim 10^3$  s) compared to the lifetime of [OI] ( $\sim 134$  s); hence, electron de-excitation will be negligible relative to spontaneous emission even for forbidden states such as [OI]. Therefore, excitation (through electron collisions) and de-excitation (through spontaneous emission or collision with the surface or other neutrals) are uncoupled in the present simulations allowing the use of two significantly different timesteps for the two models. Both routines model the dynamics using a Monte Carlo method in which representative electrons or neutrals move and probabilistically collide in space during a finite timestep. In each routine, we employ a pre-computed steady-state neutral  $\text{SO}_2/\text{O}/\text{SO}/\text{S}/\text{O}_2$  atmosphere that has negligible bulk flow velocity except in the volcanic plumes. The pre-computed atmospheric density is scaled to better match observed  $\text{SO}_2$  column densities on the dayside and to account for eclipse; however, this scaling is constant throughout a given simulation. Gas dynamics and chemistry are included only in the sense that we utilize a prescribed, pre-computed atmospheric model which included these effects. Finally, the model explicitly assumes the atmosphere is optically thin and ignores reflection off of Io's surface and photo-reactions since Io is in eclipse.

We first analyzed the problem with a 1-D code that was subsequently developed into a 3-D code. The simulation, shown schematically in 1-D in Fig. 1, used 151 grid cells in the altitude (Z) direction with a  $\Delta Z$  of 10 km. The electrons are input high in Io's  $\text{SO}_2$  and O atmosphere at 1500 km with a temperature of 5 eV. In this region, the neutral density is several orders of magnitudes lower than at the surface and the atmosphere is nearly collisionless. For the 1-D simulation, the initial vertical velocity components of all electrons are oriented toward the surface. In this model, electrons are moved only along the Z-axis and can change

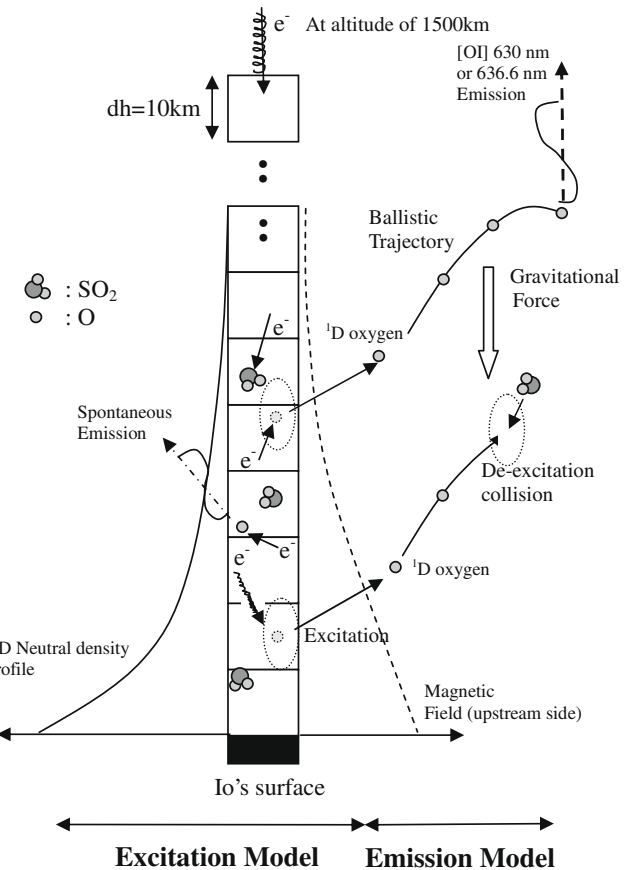


**Fig. 1.** Schematic of the computational features for the 1-D Excitation and Emission Model.

their direction and energy through collisions. The vertical neutral density profile is taken from Fig. 3 in Wong and Johnson (1996) for a solar zenith angle (SZA or  $\varphi$ ) of 30°. This model is used to examine the emission intensity ratio between [OI] and [SII] and the effect that Pele has on the [OI] emission.

Fig. 2 is a schematic depiction of our 3-D model for Io's aurora. Io is placed at the center of the computational domain which is a 9000 km  $\times$  6000 km  $\times$  6000 km box. We assume that the O number density outside the domain is small enough that any emission produced is both small and relatively uniform across the domain. The problem naturally contains two coordinate systems: one in the torus frame of reference and the other in the atmospheric frame of reference. Since the pre-computed magnetic fields are in the torus coordinate system, the electrons are moved in the torus frame of reference where the z-axis points up along the magnetic field direction at Io, the y-axis points away from Jupiter, and the x-axis points against the plasma flow. Then, in order to compute the neutral density and determine if an electron–neutral collision should occur, the electron's position vector is transformed into the atmospheric coordinate system where the z'-axis is aligned with Io north and the y'-axis points away from the Sun. Excited neutrals are also moved in the atmospheric coordinate system in order to facilitate faster computation of the local density. Finally, the emission is line-of-sight integrated in the Earth–Io coordinate system where the Z-axis is aligned with Io north and the Y-axis points away from the Earth.

The model can be summarized as follows: electrons are input at the domain boundaries and move along pre-computed magnetic field lines and can collide with a pre-computed steady state atmosphere. The excited atoms, say  ${}^1\text{D}$  O, created through electron

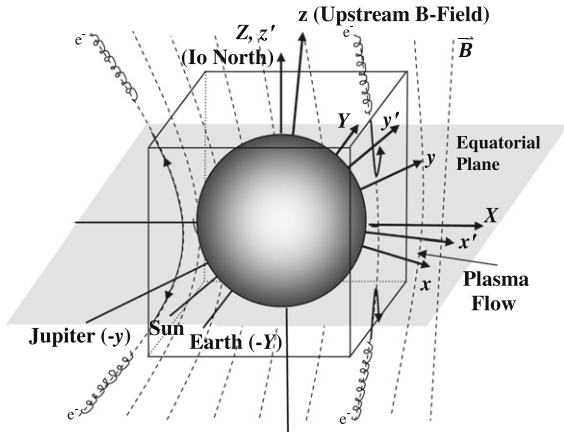


**Fig. 2.** Schematic of interaction model and illustration of geometry when Io is in eclipse. Three coordinate systems are shown: the electron transport is computed in the  $xyz$  system and the excited oxygen transport in the  $x'y'z'$  system and the subsequent emission is computed in the  $XYZ$  system. The  $xyz$  axes are aligned with the upstream magnetic field and the anti-jovian spot, the  $x'y'z'$  axes are aligned with Io north and away from the sub-solar point, and the  $XYZ$  axes are aligned with Io north and the anti-Earth spot. Io's equatorial plane ( $XY$  plane) is shown in the figure. The plasma flow is coming from the right side. Io is at the center of our simulation domain [in a box ( $9000 \text{ km} \times 6000 \text{ km} \times 6000 \text{ km}$ )]. The jovian background magnetic field (dashed lines) bends around Io.

impact of neutral O atoms are then given a thermal velocity and moved until they either collide (and quench) with molecules in the pre-computed atmosphere or emit. First, we will present the details of the pre-computed atmospheric and magnetic field models used in the present simulations before describing the models for the Excitation and Emission routines.

## 2.2. Atmospheric model

Io's  $\text{SO}_2$  atmosphere is thought to be produced by two separate physical processes: volcanic eruptions and sublimation from  $\text{SO}_2$  frost patches at the surface. In 1979, the Voyager IRIS experiment detected gaseous  $\text{SO}_2$  (Pearl et al., 1979) and it was later discovered that the dominant atmospheric component was  $\text{SO}_2$  (Ballester et al., 1990, 1994; Trafton et al., 1996; Lellouch, 1996), likely provided by active volcanoes (McGrath et al., 2000; Spencer et al., 2000; Jessup et al., 2004, 2007). In addition, ground based infrared observations suggested that there are patches of  $\text{SO}_2$  frost on the surface (Fanale et al., 1979; Smythe et al., 1979; Carlson et al., 1997; Douté et al., 2001); when the surface temperature is warm enough ( $\gtrsim 110 \text{ K}$ ) these frosts will sustain a sublimation driven  $\text{SO}_2$  atmosphere (Ingersoll et al., 1985). Therefore, in addition to the atmospheric variability from volcanic activity, the sublimation component of the atmosphere varies strongly depending on the local surface temperature and possibly on the presence of surface frost.

### 2.2.1. Model sublimation atmosphere

The sublimation atmosphere component in the current model is derived from curve-fits to the 2-D continuum gas results shown in Wong and Smyth (2000). Wong and Smyth's (2000) model considered plasma and Joule heating (but not plasma-induced chemistry), non-local thermodynamic equilibrium cooling, and photochemical reactions. Their result, which was qualitatively consistent with results of other models, showed that  $\text{SO}_2$  was the dominant atmospheric species and that the sub-solar/nightside  $\text{SO}_2$  column density ratio was  $\sim 10^3$ . However, they assumed that both  $\text{SO}$  and  $\text{O}_2$  were non-condensable and non-reactive on the surface and found that the nightside atmosphere was mainly  $\text{SO}$  and  $\text{O}_2$ .

Since Wong and Smyth's (2000) base atmospheric model did not produce satisfactory auroral morphologies, the atmospheric densities were scaled to bring the sub-solar  $\text{SO}_2$  column density more in-line with recent observations (Feaga et al., 2009) and to model the effects of eclipse. Smyth and Wong's (2004) newer atmosphere was also investigated. Because the oxygen density (and that of other  $\text{SO}_2$  dissociation products) falls off much more slowly than  $\text{SO}_2$  at high altitudes in the newer model, it was hoped that this would increase the altitude and brightness of the wake spot. However, our simulations with Smyth and Wong's (2004) atmosphere found a peak  $[\text{OI}] 6300 \text{ \AA}$  brightness that was  $\sim 2$  times higher than observed and it was found to produce an upstream auroral spot that was significantly brighter than the wake spot, counter to what is observed.

In the current model, an asymmetric  $\text{SO}_2/\text{O}/\text{SO}/\text{S}/\text{O}_2$  atmosphere is used.  $\text{S}_2$  is not included since Moses et al. (2002) found that the lifetime of  $\text{S}_2$  was short and hence significant  $\text{S}_2$  gas should only be found in the vicinity of the giant plumes; future work (Moore et al., 2010) will include  $\text{S}_2$  in the Pele-type plumes. Two different representative density profiles,  $n_{h,i}(h, \Gamma)$ , as a function of altitude were used: a dayside profile,  $n_{h,i}(h, \Gamma = 30^\circ)$ , for solar zenith angles up to the dayside/nightside transition angle,  $\varphi_{D/N}$ , and a nightside profile,  $n_{z,i}(h, \Gamma = 150^\circ)$ , for solar zenith angles greater than  $\varphi_{D/N}$  (see Fig. 6, Wong and Smyth, 2000). In order for the total column at a given SZA along the equator to match Wong and Smyth's (Fig. 5, 2000) value, the atmospheric density profiles are scaled by the normalized longitudinal variation in column density  $N_i(\varphi)/N_i(\Gamma)$  for gas species  $i$  at SZA  $\varphi$ . A continuous number density,  $n_i(h, \varphi)$ , for gas species  $i$  at altitude  $z$  and SZA of  $\varphi$  is therefore obtained by:

$$n_i(h, \varphi) = n_{h,i}(h, \Gamma) \times \frac{N_i(\varphi)}{N_i(\Gamma)} \quad (1)$$

where  $\Gamma$  corresponds to a SZA of either  $150^\circ$  or  $30^\circ$  depending on whether  $\varphi$  is greater or less than  $\varphi_{D/N}$ , respectively. For the simulations shown here,  $\varphi_{D/N}$  was set to  $90^\circ$ . Alternative values for  $\varphi_{D/N}$  were investigated, including  $120^\circ$  (the approximate shock location in Wong and Smyth's (2000) simulation), and we found little difference in the simulated emission intensity as viewed from Earth. However, abruptly switching the atmospheric profiles between dayside and nightside leads to discontinuous emission in that region. To remove the discontinuity, we used linear smoothing over  $\pm \varphi_{\text{smooth}}$  (set to  $15^\circ$ ). The density at a given altitude and SZA in this region ( $\varphi_{D/N} - \varphi_{\text{smooth}} \leq \varphi \leq \varphi_{D/N} + \varphi_{\text{smooth}}$ ) was computed by:

$$n_{h,i}(h, \varphi) = f_{\text{Day}} * n_{h,i}(h, 30^\circ) + (1 - f_{\text{Day}}) * n_{h,i}(h, 150^\circ) \\ f_{\text{Day}} = \frac{(\varphi_{D/N} + \varphi_{\text{smooth}}) - \varphi}{2 * \varphi_{\text{smooth}}} \quad (2)$$

The sensitivity of the  $[\text{OI}] 6300 \text{ \AA}$  emission intensity to the local gas density (due to quenching) requires that the  $\text{SO}_2$  density be as accurate as possible. Recent observations by Feaga et al. (2009) found that the average sub-jovian column density was  $\sim 1.5 \times 10^{16} \text{ cm}^{-2}$ ; however, the sub-solar density in Wong and Smyth's (2000) high density case (sub-solar temperature of  $120 \text{ K}$ ) is  $\sim 6 \times 10^{17} \text{ cm}^{-2}$ . Walker et al. (2010) found that a sub-solar temperature of  $115 \text{ K}$  produced column densities more in-line with Feaga's observations and that the atmosphere remains mostly in hydrostatic equilibrium even far away from the sub-solar point. Therefore, in order to reduce the Wong and Smyth  $\text{SO}_2$  gas density to a more appropriate level, we scale (on the dayside) the  $\text{SO}_2$  density at a given latitude and longitude by the ratio of the analytic hydrostatic column density assuming a sub-solar temperature of  $115 \text{ K}$  to the hydrostatic column density for a sub-solar temperature of  $120 \text{ K}$ . In order to get the  $\text{SO}_2$  density at a given location we multiply the density obtained from Eq. (1) by:

$$\frac{N_{SO_2}(T_{SS} = 115 \text{ K})}{N_{SO_2}(T_{SS} = 120 \text{ K})} = \exp\left(\frac{-4510}{T(T_{SS} = 115)} + \frac{4510}{T(T_{SS} = 120)}\right) \quad (3)$$

where  $T(T_{SS}) = (T_{SS} - 80)\cos^{0.75}(\varphi) + 80$  is the local surface temperature (see Eq. (1) in Wong and Smyth (2000)). This scaling results in a sub-solar density of  $\sim 10^{17} \text{ cm}^{-2}$ , which is in much better agreement with the observational value of Feaga et al. (2009) given that the observational density is the average value, not the sub-solar column density. Note that, by only scaling the  $SO_2$  density, the concentration of the minor species' ( $O$ ,  $SO$ ,  $S$ , and  $O_2$ ) increases. However, inclusion of electron chemistry naturally leads to an increase in the minor species concentrations as shown by Smyth and Wong (2004) and therefore the minor species concentrations obtained by the scaling are reasonable.

Since the vapor pressure of  $SO_2$  is extremely sensitive to temperatures near Io's day/night surface temperature, the sublimation atmosphere might be expected to largely collapse during eclipse. Thus, during the observation period we are modeling (the first  $\sim 10$  min of eclipse), the non-volcanic component of the atmosphere is not truly steady. Moore et al. (2009) simulated a 1-D atmospheric collapse upon ingress into eclipse with and without the presence of various non-condensable species. If there is no non-condensable, they found that the atmospheric number density 10 min into eclipse drops by an order of magnitude near the surface, but does not change above  $\sim 100$  km. However, the presence of a nominal amount of non-condensable was found to greatly slow the collapse due to the formation of a quasi-static diffusion layer near the surface. With a non-condensable present, the near-surface  $SO_2$  number density decreased only by a factor of  $\sim 4$  and did not change above 20 km. Furthermore, the rate of the atmospheric column decrease was found to slow as eclipse progressed, eventually resulting in quasi-steady atmospheric density profiles. Thus Moore et al.'s (2009) results suggest that using a steady atmosphere 5–10 min into eclipse to simulate 5 min observations should be fairly accurate.

As mentioned above, the sensitivity of [OI] emission to the local neutral density means that any asymmetry in the atmosphere should affect the emission morphology. Since the plasma "wake" enters eclipse  $\sim 210$  s before the "upstream" region, the 210 s difference in the extent of partial atmospheric collapse across Io could significantly alter the emission intensity and morphology. For example, the ratio of upstream emission intensity to downstream emission intensity might be expected to decrease since the atmospheric density (and correspondingly the quenching rate) drops more on the wake side than the upstream side. To approximate this behavior, the  $SO_2$  density computed from Eq. (1) is further scaled by the fractional drop in density versus altitude (relative to steady state) at 5 and 10 min into eclipse as computed by our 1-D DSMC collapse simulation for a pure  $SO_2$  atmosphere (Moore et al., 2009, Fig. 4a). We use the pure  $SO_2$  collapse results because the dominant possible non-condensable,  $SO$ , is most likely condensable (Baklouti et al., 2008) and any buildup during collapse of  $SO_2$  may be expected to be partially swept away by strong circumplanetary winds that develop from the dayside to the nightside (Walker et al., 2010). Over the observational time frame (Trauger et al., 1997) the wake side was in eclipse from  $\sim 5$  min post-ingress to 13 min post-ingress. Therefore, the fractional drop in density 10 min after ingress is used to scale the  $SO_2$  on the wake side at a longitude of  $\sim 51^\circ$  ( $60^\circ$  SZA). Since the upstream side was in eclipse from  $\sim 1$  min post-ingress until 9 min post-ingress, the drop in density after 5 min scales the upstream  $SO_2$  density at a longitude of  $\sim 291^\circ$  ( $60^\circ$  SZA). For longitudes in-between (e.g.  $SZA \leq 60^\circ$ ), the scaling factor is linearly interpolated between the two. Also, alteration of the circumplanetary flow from the sub-solar point to the nightside should result in only minor changes in the nightside density during the first few minutes of eclipse. There-

fore, the altitude dependent scaling factor is linearly increased from the 1-D DSMC value at a SZA of  $60^\circ$  to unity (e.g. no change in the density computed from Eq. (1)) at a SZA of  $100^\circ$ .

One might expect the atomic oxygen density to decrease early in eclipse like the  $SO_2$  density. However, unlike  $SO_2$  whose source (sublimation from frost) is dramatically reduced as the surface cools, the source of  $O$  is primarily  $SO_2$ ,  $SO$  and  $O_2$  that are dissociated by energetic plasma particles at altitudes above several kilometers where very little density change takes place during the first 10 min of eclipse. Therefore, while the near surface oxygen density will change slightly due to the  $SO_2$  bulk flow into the surface, the  $O$  density above a kilometer should remain relatively constant early in eclipse.

Due to the variable atmospheric collapse across Io, the model's sublimation atmosphere is asymmetric longitudinally on the dayside and partially onto the nightside. However, it should be noted that the model sublimation atmosphere does not include the asymmetry that results from the thermal inertia of the frost (and hence a skewed surface temperature) or from the drag of the plasma torus on Io's atmosphere. The momentum transfer from the plasma acts to reduce the upstream atmospheric scale height relative to the wake (Saur et al., 2002) which should tend to dim the emission on the upstream side relative to the wake due to increased quenching rates upstream.

### 2.2.2. Volcanic model

In addition to the above sublimation atmosphere, large active volcanoes like Pele and Tvashtar cause large local density variations in the atmosphere. Because ionian plumes can cover a region the size of an entire auroral bright spot they could be important for modeling the emission features. Our atmospheric model contains up to 14 volcanoes, listed in Table 1, known to have been active for the observation period. We used Geissler et al.'s (2004a) timeline of major eruptions (see their Fig. 26) that is based on observed surface changes in the vicinity of the volcanoes. Since some of the volcanic areas (e.g. Culann, Ra) had no image coverage or poor image quality during the 1997 HST eclipse observations, we have run cases with those plumes both active and inactive but found little variation in overall emission for such small plumes. Similarly, we ran a case with Loki inactive (as a plume source) and the emission results were unchanged except for an increase in emission in the immediate vicinity of Loki.

The simulation uses two general volcanic types, each of which can be either dayside (when the sublimation atmosphere beneath the plume is substantial, e.g. surface temperatures greater than  $\sim 110$  K) or nightside (when the sublimation atmosphere is minor). Large volcanoes with a ring radius exceeding  $\sim 400$  km and shock

**Table 1**

Active volcano list (Geissler et al., 2004a).

Plume	Longitude, latitude	Type
Kanehikili	38W, 16S	Day Prometheus
Grian (S. Karei)	16W, 2N	Day Prometheus
Amirani	117W, 24N	Night Prometheus
Tvashtar <sup>b</sup>	125W, 59N	Night Pele
Prometheus	156W, 2S	Night Prometheus
Culann	164W, 20S	Night Prometheus
Zamama	174W, 18N	Night Prometheus
Marduk	210W, 27S	Night Prometheus
Pillan	244W, 12S	Night Prometheus
Pele	256W, 20S	Night Pele
Loki <sup>a</sup>	311W, 10N	Day Prometheus
Dazhbog <sup>b</sup>	302W, 54N	Day Pele
Acala	336W, 11N	Day Prometheus

<sup>a</sup> Active, Rathbun et al. (2002).

<sup>b</sup> Assumed to be dormant for most simulations.

heights of several hundred kilometers are classified as Pele type, and we have three such plumes (Pele, Tvashtar, and Dazhbog) in the simulation. Following the work of Zhang et al. (2003, 2004), our Pele-type plumes have a virtual vent temperature of 650 K, a gas velocity of 900 m/s, and a mass flow rate of  $1.1 \times 10^4$  kg/s. Volcanoes that are smaller are simulated as Prometheus-type plumes with a ring radius of  $\sim 180$  km and a shock height of 120 km. Our Prometheus-type plumes have a virtual vent temperature of 300 K, a gas velocity of 500 m/s, and a mass flow rate of  $5.9 \times 10^3$  kg/s. Each volcano was simulated with 99.9% SO<sub>2</sub> and 0.1% O (by number) and an assumed plasma energy flux into the top of the domain of  $5 \text{ erg s}^{-1} \text{ cm}^{-2}$ ; additional parameters for each volcano type are found in Table 2. Zolotov and Fegley (1998) and Moses et al. (2002) found that the mole fraction of O in the plume vent was at most  $\sim 10^{-4}$ ; hence we used 0.1% as an upper limit. However, it was found that the assumed O mole fraction did not affect the results unless O was a significant constituent (>10%) of the plume gas. The current model does not include S<sub>2</sub> in the Pele-type plumes. This omission is acceptable because whether the plumes are composed of SO<sub>2</sub> or S<sub>2</sub> should not matter to our model's oxygen emission since the oxygen in the plumes is due to vent chemistry, not plasma chemistry in the plume itself. Furthermore, the S<sub>2</sub> present in Pele-type plumes should not result in significant increased [SII] emission since the plume density is high enough to collisionally quench the excited state. Moore et al. (2010) examines the intense band emission from the S<sub>2</sub> B  ${}^3\Sigma_u^- \leftarrow X^3\Sigma_u^-$  transition which emits from  $\sim 2800$  to  $6400 \text{ \AA}$  and the implications on giant, S<sub>2</sub>-rich plume activity.

The volcanic plumes were pre-computed using our existing volcanic model (Zhang et al., 2003, 2004) and then overlaid onto the sublimation atmosphere, neglecting the gas dynamic interactions with nearby plumes and the non-uniform sublimation atmosphere. At a given location inside a simulated plume's domain, the model density was computed by superimposing the plume simulation density and the sublimation atmosphere density. Inside the plume's ring radius,  $S_{\text{Ring}}$ , it was assumed that the non-uniform sublimation atmosphere gas flows would have a negligible effect on the gas properties and therefore the model gas densities were set to the plume gas densities. Outside of the plume's ring radius the plume simulation density,  $n_p$ , is reduced exponentially based on the distance along the surface,  $S$ , and a plume-type dependent length scale,  $L_p$ :

$$N = n_p \times \exp\left(-\frac{S - S_{\text{Ring}}}{L_p}\right) \quad (4)$$

We assumed that  $L_p$  was equal to 30 km for Prometheus-type plumes and 90 km for Pele-type plumes. This offsets the contribution of the far-field sublimation atmosphere that is accounted for in the dayside plume simulations and limits "double counting" of the sublimation atmosphere inside the plume domain and consequent density jumps across the outer plume boundary. Other properties (such as temperature) are mass-averaged such that a given property,  $\xi$ , inside a plume domain would be equal to

$$\xi = \frac{\xi_p n_p + \xi_S n_S}{n_p + n_S} \quad (5)$$

**Table 2**  
Volcano parameters.

Type	$T_{\text{surf}}$ (K)	$V_{\text{vent}}$ (m/s)	$T_{\text{vent}}$ (K)	$n_{\text{vent}}$ (#/cm <sup>3</sup> )	$N_{\text{centerline}}$ (#/cm <sup>2</sup> )	$R_{\text{ring}}$ (km)	$H_{\text{shock}}$ (km)
Day Prometheus	112	500	300	$5 \times 10^{13}$	$1.1 \times 10^{18}$	175	110
Night Prometheus	90	500	300	$5 \times 10^{13}$	$2.2 \times 10^{18}$	80	40
Day Pele	111	900	650	$5 \times 10^{13}$	$1.4 \times 10^{18}$	580	315
Night Pele	90	900	650	$5 \times 10^{13}$	$1.4 \times 10^{18}$	580	315

where  $n$  is the number density and the subscript "P" refers to the simulated plume value and "S" refers to the sublimation value (computed from Eqs. (1)–(3)).

Representative plots of the final composite model atmosphere are shown in Fig. 3. Fig. 3a shows density profiles (for clarity, only SO<sub>2</sub> and O profiles are shown) at a SZA of 30° obtained from curve-fits to the profiles of Wong and Smyth (2000). As can be seen, the scaled SO<sub>2</sub> density profiles now depend on longitude because the time since ingress varies with longitude. The upstream side is characterized by the 322° longitude (30° SZA) curve which has a higher density than the wake side curve (22° longitude). Also, note that both scaled curves have been reduced by a factor of  $\sim 10$  in order to bring the sub-solar column more in-line with recent observations, as discussed above Eq. (3). Furthermore, the profiles are exponentially extended for altitudes above 500 km. If we set the number density above 500 km to zero instead of extrapolating, the emission morphology remains essentially the same and the overall intensity becomes slightly weaker. The SO<sub>2</sub> number density at the surface and in two altitudinal slices near each limb (picked to highlight plumes) is shown from nearly Earth view (rotated 12° to show Pele) in Fig. 3b. Several plumes are visible; note that near the surface underneath Pele the SO<sub>2</sub> density is very low. The atmospheric scale height in the Pele slice (on the nightside) is seen to be larger than in the Kanehikili slice (on the dayside) demonstrating the need for smoothing the dayside and nightside profiles (Eq. (2)) near the poles. Fig. 3c shows the SO<sub>2</sub> column density as a function of longitude and latitude. Dashed lines indicate the longitudes ( $\text{SZA} = 90^\circ \pm 15^\circ$ ) over which the dayside and nightside density profiles are linearly averaged. Longitudinal asymmetry in the SO<sub>2</sub> column is seen due to the inclusion of partial eclipse. Also, it is seen that the plumes contribute locally to the column of the background sublimation atmosphere.

### 2.3. Excitation model

In the Excitation model, the plasma torus electrons can interact with the atmosphere of SO<sub>2</sub>, O, SO, and O<sub>2</sub> described above in Section 2.2 (note that we do not currently include electron interactions with S atoms). Currently, the model only includes the thermal ( $\sim 5$  eV) electrons in the plasma torus; previous work concluded that energetic ( $\sim 10$  keV) non-thermal electrons do not produce significant emission (Bhardwaj and Michael, 1999a). A future paper will examine the contribution of lower energy (30 eV) non-thermal electrons based on Oliversen et al.'s (2001) suggestion that they might cause the short-term fluctuations in [OI] 6300 Å emission. Since the mean-time between electron–neutral collisions is long compared to the interaction time during a collision, the Excitation routine decouples the electron motion, in which electrons move along the magnetic field lines, from the collision process, when an electron might undergo a collision. From the Excitation model, a steady-state spatial distribution of <sup>1</sup>D oxygen is obtained.

Since the electrons move in space (not on a grid), the magnetic field must be interpolated from the pre-computed magnetic field data. In order to speed up this interpolation, the pre-computed magnetic field data (given on Combi et al.'s (1998) unstructured Cartesian grid) is initially interpolated to our Cartesian grid having

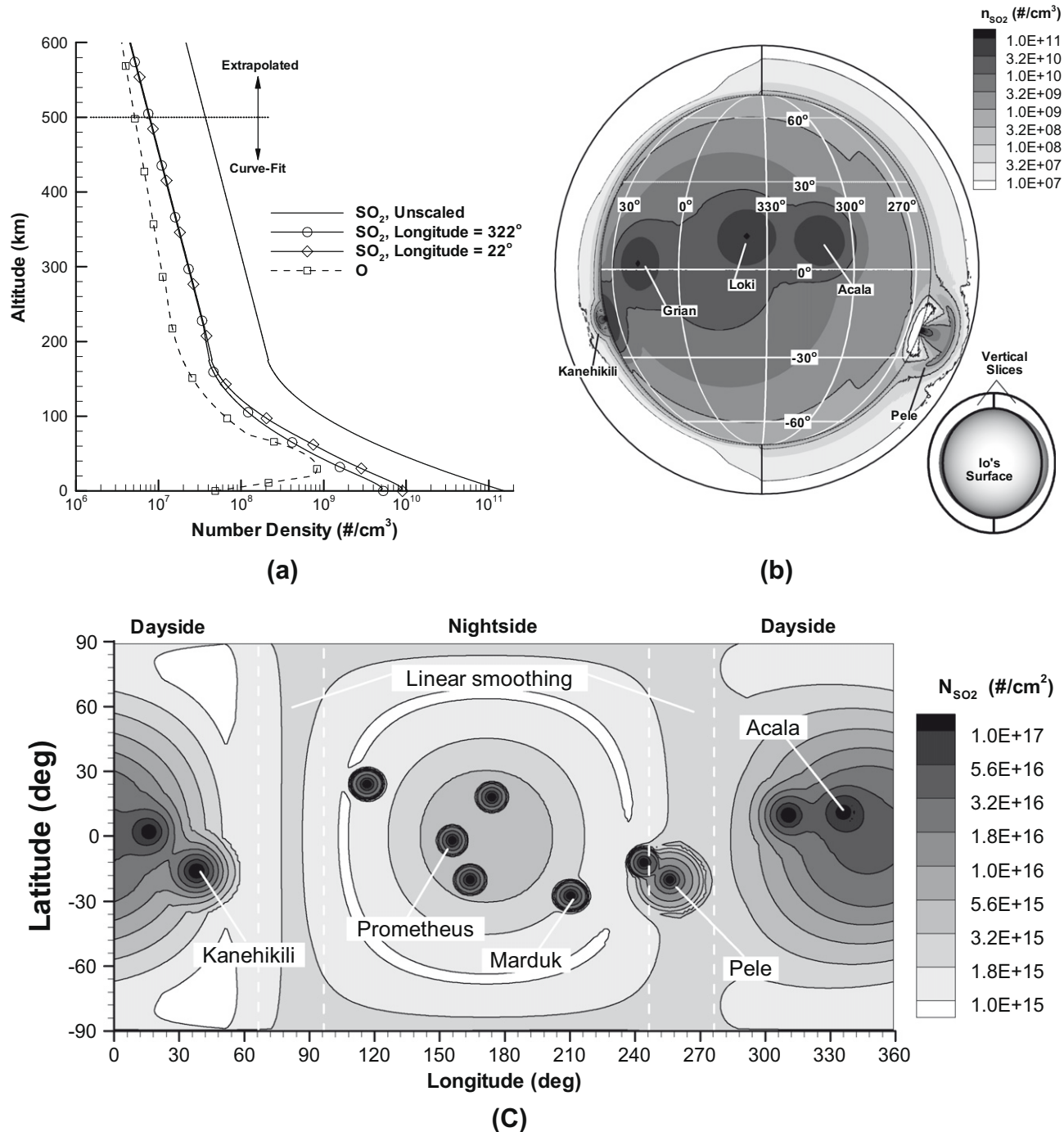


**Fig. 3.** The simulation atmosphere based on curve-fits of Wong and Smyth's (2000) data with superimposed plumes (Zhang et al., 2004). (a) Reproduction of the sublimation number density profiles for SO<sub>2</sub> and O at 30° SZA. The extension to higher altitudes as well as the result of scaling the SO<sub>2</sub> density which increases the near surface scale height to ~30 km on the dayside. (b) SO<sub>2</sub> number density near the surface (~100 m) and in vertical slices near each limb cutting through two plumes (Pele and Kanehikili). Contour lines are drawn every other level for clarity. The averaging of the dayside and nightside profiles is especially apparent near the poles – the Pele slice shows the nightside atmospheric profile (with a larger scale height due to increased plasma heating at lower altitudes) and the Kanehikili slice shows the dayside. (c) Longitude-latitude plot of SO<sub>2</sub> column density for our full atmosphere model with the base case plumes active (Table 1) and accounting for asymmetrical partial collapse. The sub-solar SO<sub>2</sub> column density is  $5 \times 10^{16}$  cm<sup>-2</sup> and the average sub-jovian SO<sub>2</sub> column density is  $1.2 \times 10^{16}$  cm<sup>-2</sup>. The region over which dayside (SZA = 30°) and nightside (SZA = 150°) profiles are averaged is marked by dashed lines.

a cell size  $\Delta X = \Delta Y = \Delta Z = 60$  km. The magnetic field is then linearly interpolated from the eight surrounding Cartesian grid points. Our Cartesian grid is also used to bin emission events for output visualization. The time step for each electron is determined by the electron energy and the local density so that the fastest electrons move less than one cell (so that magnetic mirroring is accurately simulated) and collide on average less than once per timestep.

### 2.3.1. Electric and magnetic fields

Complex interactions between Io's ionosphere and the jovian magnetosphere (Neubauer, 1998) make it difficult to create a comprehensive MC simulation of Io's auroral emission. The Galileo spacecraft showed that the ionosphere around Io is strongly perturbed by the plasma flow and that the jovian magnetic field is bent in the vicinity of Io (Frank et al., 1996). There are several

sophisticated MHD models for the interaction of Io with Jupiter's magnetosphere that are reasonably consistent with the observations of Pioneer 10, Voyager 1 and Galileo, e.g. Kivelson et al. (2001), Combi et al. (1998), Neubauer (1998), and Linker et al. (1991, 1998).

The plasma's bulk motion relative to Io,  $\vec{v}_{lo}$  (=57 km/s), and the jovian magnetic field,  $\vec{B}_J$ , establish a corotational electric field:

$$\vec{E}_{corot} = -\vec{v}_{lo} \times \vec{B}_J \quad (6)$$

We use the magnetic field (and drift velocity field) provided by Combi (see Fig. 1c, Combi et al., 1998). Their 3-D MHD model considers the ion mass loading, ion-neutral drag, no intrinsic ionian magnetic field, and can qualitatively explain the measurements made during Galileo's flyby of Io as noted previously. Note that it was necessary to rotate their simulated magnetic field in order for the upstream magnetic field to be oriented correctly relative to Io north at the time of the observation. This rotation introduces additional approximations, but, since they used a uniform atmosphere model, rotation of the field relative to Io's geographical coordinates should be self-consistent with the model of Combi et al. (1998). However, our model is limited because large atmospheric features (such as Pele) do not perturb the modeled magnetic field.

### 2.3.2. Electron motion

It is convenient to divide an electron's motion into two parts: a velocity component parallel to the magnetic field ( $\vec{v}_{||}$ ) and another component perpendicular to it ( $\vec{v}_{\perp}$ ). Near Io, the perpendicular component of the drift velocity ( $v_{\perp,drift} = (E \times B)/B^2$ ) becomes large relative to its value far from Io and thus there exists a bulk electron flow around the surface in addition to Io's relative motion through the plasma torus. The motion of electrons can be described by

$$\vec{v}_e = \frac{(\vec{E}_{corot} - \vec{E}_{pol}) \times \vec{B}_J}{B_J^2} + \vec{v}_{||} \quad (7)$$

where  $\vec{E}_{pol}$  is the polarization electric field. Other drifts such as the gravitational drift,  $\vec{v}_g = m(\vec{g} \times \vec{B})/qB^2$ , and field curvature drift,  $\vec{v}_{curve} = m(R_c \times \vec{B})(v_{||}^2 + \frac{1}{2}v_{\perp}^2)/(qR_c^2B^2)$  (where  $m$  is the charged particle mass,  $q$  is the charge,  $g$  is the gravitational acceleration, and  $R_c$  is the radius of curvature of the magnetic field), are neglected since they are less than ~10 m/s near Io for typical thermal electrons and reasonable magnetic fields. Furthermore, near Io the corotational electric field is nearly canceled by the polarization field and so the velocity component perpendicular to the magnetic field is very small compared to the parallel velocity (Saur et al., 2000).

We exclude gyration motion of the electrons because in the plasma torus near Io, a typical gyration radius,  $r_{gyro} = v_{\perp}m/(q|\vec{B}|)$  (where  $|\vec{B}|$  is the magnitude of the perturbed jovian magnetic field), is several meters (<7 m for 7.5 eV electrons), which is much smaller than the atmospheric scale height and length scales present in volcanoes. Because  $r_{gyro}$  is so small, it is reasonable to neglect the gyration and just move the electrons solely along the magnetic field lines. However, note that the total electron velocity,  $v_e$ , is used to compute the collision probability. Also, note that the ratio of the gyrofrequency to the electron collision frequency, i.e. the Hall parameter,  $\beta$ , is given by

$$\beta = \frac{\omega_c}{v_{e-n}} \approx \frac{q|\vec{B}|/m_e}{n_n \sigma_{tot}(\bar{v}_r) \bar{v}_r} \quad (8)$$

where  $n_n$  is the local neutral number density,  $\bar{v}_r$  is the relative velocity between the electrons and neutrals ( $v_r \approx v_e$ ),  $\sigma_{tot}(v_r)$  is the total collision cross section between the electrons and neutrals as a function of relative velocity, and the bar represents the average value. Near the surface at the sub-solar point  $\beta \approx 3$ , and is much larger elsewhere. Therefore the electrons do not diffuse off their field lines

(through collisions) and an average drift velocity for the electron's motion can be used.

To model the helical motion of the electron along the magnetic field line and account for the magnetic mirror effect, we introduce the adiabatic invariant magnetic moment,  $\mu_{mag}$ :

$$\mu_{mag} = \frac{\frac{1}{2}m_e v_{\perp}^2}{|\vec{B}|} \quad (9)$$

We store  $\mu_{mag}$  for each electron and update it when the electron undergoes a collision. If the magnetic field strength increases smoothly along the field line, Eq. (9) can be rearranged to yield the following condition for the local pitch angle:

$$\sin(\alpha) = \sin(\alpha_{Initial}) \sqrt{\frac{|\vec{B}|}{|\vec{B}_{Initial}|}} \quad (10)$$

where the subscript 'Initial' denotes the value at the location of the last collision (or where the electron was created if it has never undergone a collision), and  $\alpha$  is the pitch angle of the electron defined by  $\tan(\alpha) = v_{\perp}/v_{||}$ . Note that the electron velocity parallel to the magnetic field is zero at the mirror point; therefore,  $\alpha = 90^\circ$ . Hence, the magnitude of the magnetic field required to reflect the electron,  $|\vec{B}_{mirror}|$ , can be obtained by rearranging Eq. (10):

$$|\vec{B}_{mirror}| = \frac{|\vec{B}_{Initial}|}{\sin^2(\alpha_{Initial})} \quad (11)$$

In the simulation, the electron's velocity parallel to the magnetic field is reversed when the local magnetic field is within 0.005% of  $|\vec{B}_{mirror}|$ .

### 2.3.3. Electron collision model

Elastic, ionization, attachment and excitation electron–neutral (atomic or molecular) interactions were considered through the use of energy dependent cross sections for each species. Table 3 shows the collision processes included for each species and the corresponding references used. For the cross sections, when a reference did not specify an equation to use, curve-fits were done to the cross section data shown. Many of the included electron impact cross sections as functions of energy for SO<sub>2</sub> and O are shown in Fig. 4a and b. Note that we do not include vibrational and rotational electron excitation of SO<sub>2</sub>, SO, or O<sub>2</sub> in the model since the cross sections for these interactions are relatively small, especially above 1.96 eV which is the minimum electron energy that can excite [OI] 6300 Å. Furthermore, while we do include the strong multiplets in EUV and FUV, we do not include most of the EUV and FUV SO<sub>2</sub>–electron impact dissociative-excitation cross sections (e.g. OI (1040 Å, 1027 Å, etc.) or SII (998 Å, etc.)) because the cross sections were small (~10<sup>-19</sup> cm<sup>2</sup>) and the threshold energies were large (>30 eV). In addition, we do not include SO<sub>2</sub> dissociation into un-ionized ground-state products because detailed cross section data were unavailable; however, note that SO<sub>2</sub> dissociation into SO(Å<sup>3</sup>Π) and O(<sup>3</sup>P) (resulting in the MUV1 spectral feature) as well as into excited OI, OII, SI, and SII is included (see Table 3). Bhardwaj and Michael (1999b) found that if SO<sub>2</sub> has a similar ratio of dissociation to excitation cross section as O<sub>2</sub>, N<sub>2</sub>, or H<sub>2</sub>O, then the SO<sub>2</sub> dissociation cross section was only ~3% of the total cross section. Hence the effect of dissociation of SO<sub>2</sub> into ground-state products should be relatively minor and can be neglected. Finally, several cross sections for electronic excitation of oxygen atoms are neglected because their cross sections were small (~10<sup>-18</sup> cm<sup>2</sup>) and their threshold energies relatively high (~20 eV).

While most electron collisions with neutrals are elastic, they are still important since they randomize the electron trajectories (up or down along the field lines) and can trap electrons in the wake

**Table 3**

Electron–neutral collision processes for neutrals initially in the ground state. Emission wavelength(s) (in Å) are indicated in parenthesis.

Collision process	Reaction products, excluding e <sup>-</sup>	Reference
SO <sub>2</sub> elastic	SO <sub>2</sub>	Bhardwaj and Michael (1999b)
MUV1	SO(Å <sup>3</sup> Π) + O( <sup>3</sup> P) (2385–2670)	Ajello et al. (2002)
MUV2	SO <sub>2</sub> (Å <sup>1</sup> A <sub>2</sub> ) ; SO <sub>2</sub> (B <sup>1</sup> B <sub>1</sub> ) (2670–6000)	Ajello et al. (2002)
SO <sub>2</sub> electronic excitation	Č + Ď; Ě + Ě; Ĝ + Ī; Ħ	Bhardwaj and Michael (1999b)
SO <sub>2</sub> ionization	SO <sub>2</sub> <sup>+</sup>	Bhardwaj and Michael (1999b)
SO <sub>2</sub> dissociative ionization	SO <sup>+</sup> ; O <sup>+</sup> ; O <sub>2</sub> <sup>+</sup> ; S <sup>+</sup>	Bhardwaj and Michael (1999b)
SO <sub>2</sub> dissociative attachment	SO <sup>-</sup> ; O <sup>-</sup> ; S <sup>-</sup>	Bhardwaj and Michael (1999b)
SO <sub>2</sub> dissociative-excitation	OI (1304); OI (989); SI (1479); SI (1900); OII (834); SII (911); SII (1204)	Bhardwaj and Michael (1999b)
O <sub>2</sub> <sup>a</sup>	O <sub>2</sub>	Szmytkowski et al. (1996)
SO <sup>a</sup>	SO	Joshi pura and Gangopadhyay (2008)
O elastic	O	Itikawa and Ichimura (1990)
O electronic	2p <sup>4</sup> <sup>1</sup> D (6300, 6364, 6392) 2p <sup>4</sup> <sup>1</sup> S (2958, 2972, 5577) 3s <sup>3</sup> S <sub>0</sub> (1304) 3p <sup>3</sup> P (1128) 3d <sup>3</sup> D <sub>0</sub> (1027) 4p <sup>3</sup> P (1003) 3s' <sup>3</sup> D <sub>0</sub> (989) 3s'' <sup>3</sup> P <sub>0</sub> (878)	Itikawa and Ichimura (1990) Itikawa and Ichimura (1990)
O ionization	O <sup>+</sup>	Itikawa and Ichimura (1990)

<sup>a</sup> Treated total scattering cross section as elastic.

region or allow them to penetrate deeper into the higher magnetic field upstream of Io. Due to the importance of scattering, electron–O<sub>2</sub> and electron–SO elastic collisions are included via their reported total scattering cross sections. However, since O<sub>2</sub> and SO are relatively minor constituents, we neglect the electron energy degradation due to inelastic collisions with these minor species. Degradation of high-energy electrons occurs mainly via ionization of SO<sub>2</sub> which produces lower energy secondary electrons which are tracked. On the other hand, attachment and excitation (e.g. excitation of atomic oxygen to <sup>1</sup>D) is important for low-energy electrons. This implies that there is an energy cascade from high-energy electrons to low-energy secondary electrons which then tend to scatter off the atmosphere through elastic collisions and/or undergo attachment or emission reactions. Any electron which reaches Io's surface is assumed to attach to Io and is removed from the computation. This surface sticking tends to occur predominately in regions with very low neutral column density and for very energetic electrons (>100 eV), whose total cross sections are small.

Due to the lack of available SO<sub>2</sub> and SO cross sections for direct creation of [OI] 6300 Å emission by electron impact dissociation, we consider only electron impact excitation of atomic oxygen as the source for 6300 Å emission. Thus, our resulting emission should be considered a lower bound since Oliversen et al. (2001) reported that the [OI] emission line width implied that a non-trivial amount of the emission was produced via electron impact dissociation. Retherford (2002) argued that emission from O, SO<sub>2</sub>, and SO may be comparable; therefore, it is not unreasonable to expect that our total simulated emission might be ~1/3 of the observed value.

When an electron (with a known velocity,  $v_e$ , and energy,  $E_e$ ) is within our domain, we determine whether it has an electron–neutral collision in time interval  $\Delta t$  by comparing a random number ( $0 < R_{\#} < 1$ ) with the total collision probability,  $P_{coll,tot}(E_e)$ :

$$P_{coll,tot}(E_e) = 1 - \exp\left(-\Delta t \sum_i^{N_s} n_i \sigma_{tot-i}(E_e) v_{e-i}\right) \quad (12)$$

Here the subscript  $i$  denotes the target species (SO<sub>2</sub>, O, etc.),  $N_s$  is the total number of species in the model,  $\sigma_{tot-i}(E_e)$  is the total interaction cross section for species  $i$  for an electron with energy  $E_e$ ,  $n_i$  is the target particle local number density, and  $v_{e-i}$  is the relative velocity between the electrons and the target molecules, which is

taken as equal to  $v_e$ . The Monte Carlo method then compares a random number to the computed collision probability, and if

$$R_{\#} < P_{coll,tot}(E_e) \quad (13)$$

then the electron collides with a random target particle in that cell. To determine which species the electron collides with, another random number is drawn and compared to the cumulative relative probability of collision for each species,  $P_{coll,i}(E_e) = \sum_k^i [n_k \sigma_{tot-k}(E_e)] / \sum_k^{N_s} n_k \sigma_{tot-k}(E_e)$ , where  $k$  is a dummy index. If the random number is less than  $P_{coll,i}(E_e)$  and greater than  $P_{coll,i-1}(E_e)$ , then the electron collides with the  $i$ th species. The collision type (ionization, excitation, etc.) is determined similarly, by comparing a third random number to the cumulative probability for each reaction,  $r$ , for the selected species:  $\sum_k^r \sigma_{RxN-k}(E_e) / \sigma_{tot-i}(E_e)$ . To avoid the expense of computing the energy-dependent interaction cross sections and total interaction cross sections for each electron every timestep, we pre-compute the cross sections for a set of several thousand electron impact energies with a fine energy step ( $\Delta E = 0.02$  eV) and tabulate the values.

After the collision the electron energy is changed appropriately and the velocity vector direction (pitch angle) is randomized, resulting in a new helical angle and magnetic moment. However, we leave the electron on the same field line because the gyration radius is small compared to the spatial gradients in the magnetic field. In general, it is necessary to have the differential scattering cross section,  $\frac{d\sigma}{d\Omega}$ , for each collision process in order to pick the electron post-collision velocity properly; however, at low energies (several eV) the scattering is approximately isotropic. Since the penetration depth of the electrons into the atmosphere is sensitive to the differential cross section, it was important to correctly model the scattering angle distribution of the dominant collision process: elastic electron–SO<sub>2</sub> collisions. In this paper, for elastic electron–SO<sub>2</sub> collisions, we curve-fit Gulley and Buckman's (1994) measured differential scattering cross section data at various electron energies. If an elastic electron–SO<sub>2</sub> collision occurs, the resultant scattering angle is sampled from the differential scattering curve at the nearest energy. All other electron–neutral collisions, including inelastic electron–SO<sub>2</sub> collisions, are assumed to scatter isotropically.

Secondary electrons generated by ionization are given a kinetic energy determined by the method of Bhardwaj and Michael

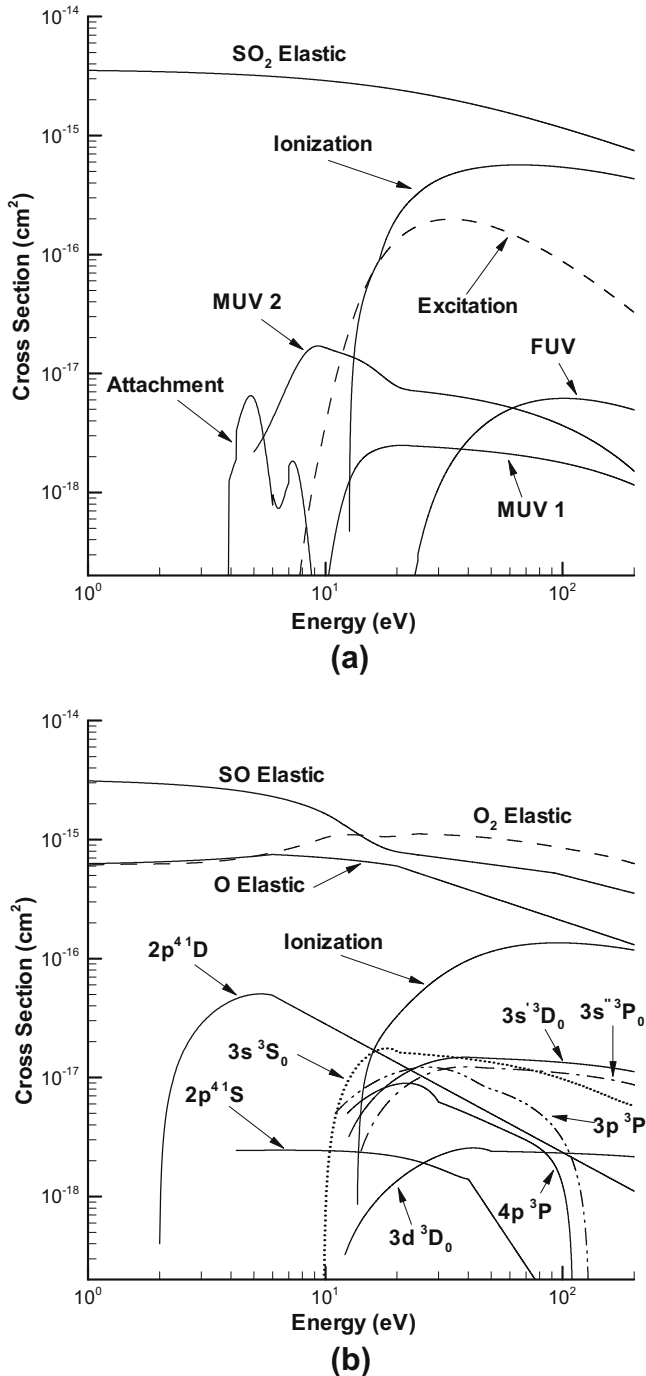


**Fig. 4.** The cross sections of all inelastic and elastic processes (Table 3) considered for (a) the dominant species, SO<sub>2</sub> and (b) the minor species O, SO, and O<sub>2</sub>. In (a) the ionization cross section is obtained by summing the cross section for production of SO<sub>2</sub><sup>+</sup>, SO<sup>+</sup>, S<sup>+</sup>, O<sup>+</sup>, O<sub>2</sub><sup>+</sup> and the excitation cross section is obtained by summing dissociative-excitation to OI(1304 Å, 989 Å), SI(1479 Å, 1900 Å), OII(834 Å), and SII(911 Å, 1204 Å). In (b) the excitation cross sections (2p<sup>4</sup> 1D, etc.) are for O and the ionization cross section is for the production of O<sup>+</sup> from O atoms.

(1999b) and a random pitch angle. Once the energy of the secondary electron has been determined, the primary electron energy is set by subtracting the energy of the secondary electron and the ionization potential from the initial energy of the primary electron. When electron attachment occurs, we simply remove the electron. Finally, each time a <sup>1</sup>D oxygen excitation event occurs, the location and velocity of the electron is stored for use in the Emission Model.

### 2.3.4. Electron input model

Only thermal electrons from the plasma torus are modeled in the current simulations. The contribution of non-thermal electrons to direct excitation of atomic oxygen to the <sup>1</sup>D state (the only <sup>1</sup>D excitation mechanism considered here) should be very small. First, the excitation cross section decreases with increasing energy above ~5 eV and, at ~100 eV, is an order of magnitude smaller than the peak value (Fig. 4b). Furthermore, the non-thermal electron density (at energies below 100 eV) is significantly smaller than the density of thermal electrons (Oliversen et al., 2001). Therefore the non-thermal electron component, due to its lower excitation cross section and density, should not significantly contribute to the <sup>1</sup>D excitation relative to the thermal contribution.

In order to properly model the input conditions along the domain boundaries, we must determine if we need to account for the flux tube depletion across Io. If the flux tube depletion is negligible, electrons can be input uniformly along the top and bottom domain boundaries; however if it is large, the electrons cannot be input uniformly across Io. To estimate the amount of depletion, we examine an electron's round trip motion to the torus "edge" and back to Io's atmosphere where the flux tube terminates. The electron must then scatter off the atmosphere if it is to remain in the flux tube as the end of the flux tube crosses Io. Moreover, electrons created from ionization processes may leave the atmosphere along the flux tube in which they were created.

This model of the flux tube depletion is similar to Rutherford (2002) and Rutherford et al. (2003) analysis where he compared the time scales for a flux tube to cross Io and for an electron to complete a round trip to the torus edge and back and concluded that most of the flux tube energy would be deposited as it crossed Io. We assume that the torus scale height is  $\approx\sqrt{2}R_J$  (Bagenal and Sullivan, 1981; Bagenal, 1985) and a plasma velocity across Io's poles of 7 km/s (Saur et al., 2002) is used, implying a travel time across Io of  $\approx 2R_{Io}/v_{plasma} \approx 520$  s. For  $T_e = 5$  eV ( $E_e = 7.5$  eV) and an isotropic pitch angle distribution, the average parallel velocity,  $\bar{v}_{||}$ , is 1035 km/s since  $|\bar{v}_e(\bar{E}_e)| \approx 1625$  km/s ( $\bar{v}_{||} = |\bar{v}_e| \int_0^{\pi/2} \cos(\alpha) d\alpha / \int_0^{\pi/2} d\alpha$ ). We assume that the electron temperature far from Io is constant; therefore, since the effect of the perturbed magnetic field around Io is small,  $\bar{v}_{||}$  remains approximately constant and the average electron travel time to the torus edge and back to Io (at the torus equator) is  $2\sqrt{2}R_J/\bar{v}_{||} \approx 190$  s. Therefore, this implies that, in order to reach the wake, the typical electron traveling across Io must either scatter off Io's atmosphere or be mirrored off the magnetic field.

We take the analysis one step further and simulate the partial depletion of the flux tube by modeling the electron scattering off Io's atmosphere. Fig. 5 shows a schematic diagram of the plasma flow past Io with Io at its maximum magnetic latitude (~10°) in the torus. The electron path angles are exaggerated for clarity. In Fig. 5 the line with square symbols (line a) is the path of an average thermal electron heading north that just misses Io upstream, travels to the northern torus edge and back to Io, and then scatters off the atmosphere back towards the torus edge. If it scatters all these times or is lost but creates another electron via ionization, then it (or its daughter) will reach the wake. The line with circles (line b) represents the electron heading south passing upstream of Io which then proceeds to scatter off the southern "edge" of the torus and the southern atmosphere until it reaches the wake. In the figure, there is no significant depletion of the flux tube in region I because an average electron in the region must have originated further upstream than the electron on the (b) line, as illustrated by the dashed line. On the other hand, the electron number density and mean energy will be depleted in region II (though for the figure we have assumed the energy depletion is small) because some

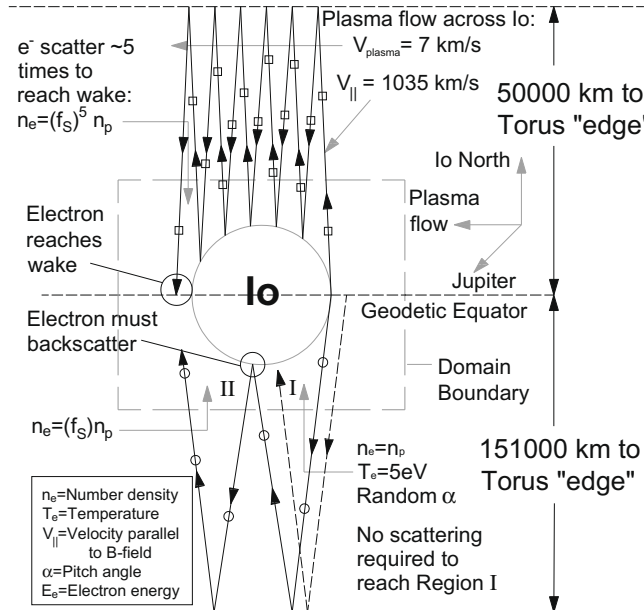


**Fig. 5.** Schematic diagram of plasma flow past Io at its maximum latitude in the torus. The plasma velocity across Io is assumed to be 7 km/s and the electron temperature is assumed to be constant. Two average electron paths are shown: one just missing lo upstream and heading north, the other heading south. Note that the electron path angles are exaggerated for clarity and not inclined by the Alfvén angle. There is little depletion of the flux tube in region I because the average electron passing through there originates further upstream than the solid lower electron path, as indicated by the dashed electron path.

fraction of electrons,  $f_j = n_{e,OUT,j}/n_{e,IN,j}$  ( $j = N$  for north and  $S$  for south), will scatter off the atmosphere and the rest will either undergo attachment or impact Io. If the fraction lost can be considered roughly constant across Io, then after  $K$  scattering events, the flux tube number density will be  $(f_j)^K n_p$ , where  $n_p$  is the electron density in the plasma far upstream. Similarly, the average energy of the electrons will be  $(f_{e,j})^K \bar{E}_p$ , where  $f_{e,j}$  is the fraction of energy remaining after scattering once and  $\bar{E}_p$  is the average electron energy upstream.

Fig. 5 shows that for Io's northern-most latitude in the plasma torus ( $\sim 10^\circ$ ), an electron reaching the wake from the north would have had to scatter  $\sim 5$  times (depending on its pitch angle and energy), compared to only once for electrons reaching the wake from the south. Thus if the fraction scattered per bounce were the same for the north and south, then fewer electrons would reach the wake from the north side of Io when Io is north of the torus equator (and vice versa when Io is south of the torus equator). This electron flux imbalance should tend to make the wake brighter in one hemisphere based only on Io's position in the torus. Furthermore, note that the fraction scattered per bounce would probably differ if the atmospheric number density was not roughly equal in the south and north. This implies, for example, that the wake morphology might change substantially if Tvashtar is active or inactive.

The flux tube depletion is modeled by initializing the electrons randomly in the plasma torus upstream (out to 36,000 km) of our simulation domain with a thermal energy distribution and an isotropic pitch angle distribution. Since the electrons are assumed to be in equilibrium, the plasma is effectively collisionless (in the Boltzmann equation the collision integral is zero) and we do not need to perform collisions upstream of our domain allowing us to efficiently move the randomly positioned electrons to their starting position along the domain boundary. Once inside the domain, the electrons are allowed to collide and convect downstream (with the local drift velocity) while moving along the magnetic field lines.

When an electron exits our domain along the top and bottom boundaries it is assumed to travel to a fixed, artificial torus “edge” set at  $\pm \sqrt{2}R_J$  from the torus equator, off which the electron mirrors instantaneously, and then proceeds to travel back to the simulation domain. During the electron's transit of the torus, electron-ion collisions are computed which alter its pitch angle but not energy. We investigated the effect of including re-thermalization of the electrons (through electron-electron collisions) and found little change in both the [OI] emission and the overall electron energy deposition. This is most likely because for nearly every low energy electron which gained energy through re-thermalization, there was a high energy electron which lost energy. It was also assumed that the electrons equilibrate (in terms of helical angle) in the plasma torus away from Io's perturbation of Jupiter's magnetic field. This should be reasonable because the mean time between collisions (electron-electron and electron-ion,  $\sim 74$  s, Sittler and Strobel, 1987) is long compared to the (average) transit time spent near Io ( $6R_{Io}/\bar{v}_{||} \sim 10$  s), but short compared to the (average) transit time to the torus edge and back ( $\sim 190$  s). Furthermore, while a given electron's velocity parallel to the magnetic field changes during transit of the torus, we assume that the electron's drift velocity (relative to Io) that it had upon leaving the domain remains constant. The electron continues to convect downstream until it leaves the domain downstream at the  $X = -3000$  km plane. We also automatically remove any electrons with  $E_e < 1.9$  eV because the activation energy of [OI] is 1.96 eV.

As described earlier, we assume that the electrons are thermalized away from Io's perturbation of the magnetic field. Therefore, when electrons re-enter the domain they are first given a random, isotropic pitch distribution at a magnetic field magnitude of  $|B_{Initial}| = |B_j| = 1835$  nT (Combi et al., 1998) and Eq. (8) is then used to adjust the pitch angle based on the local magnetic field at the point of entry into the domain of the electron. If the local magnetic field at the domain boundary exceeds  $|B_{mirror}|$  for the electron, then the electron is assumed to have been reflected before it reached the domain boundary. These reflected electrons then drift further downstream as they travel to the torus edge and possibly back to the domain boundary, where the process of obtaining a new pitch angle is repeated.

#### 2.4. Emission Model

After completion of the electron transport and collision simulation in the Excitation model, we next compute the [OI] emission in the Emission Model, again using a Monte Carlo process. Modeling the emission in this way is necessary since the emission is due to a forbidden transition (primarily via magnetic dipole transitions) from the  ${}^1D$  state to the  ${}^3P$  state and the lifetime of the excited oxygen is very long. This long lifetime means that transport of the excited oxygen and collisions, which de-excite (quench) the oxygen before spontaneous emission occurs, are critical to the emission intensity/morphology.

Excited oxygen atoms in the  ${}^1D$  state obtained from the Excitation Model are assumed to start with an initial thermal velocity based on the local atmospheric temperature (Fig. 3 from Wong and Smyth (2000)) and, if the atom is in a volcanic plume, a bulk velocity and temperature based on the pre-computed local gas velocity and temperature in the plume. That is, it is assumed that the O atoms are in thermal equilibrium with the surrounding local atmosphere before they are excited by electron impact. The velocity of the excited oxygen is then altered via hard sphere collision dynamics with the electron to approximate the recoil due to the electron impact (this is a small effect). The subsequent O atom trajectory is then simulated with an adaptive timestep much smaller than both the local mean time between molecular collisions and the mean lifetime of [OI]. After moving the excited oxygen, the

probability that the excited oxygen collides with another neutral is again given by

$$P_c \approx 1 - \exp\left(-\Delta t \sum_i n_i \sigma_{o^*-i} v_{o^*-i}\right) \quad (14)$$

where  $\sigma_{o^*-i}$  is the hard sphere collision cross section between the excited oxygen (using the effective diameter of ground state oxygen) and the  $i$ th species (Bird, 1994) and  $v_{o^*-i}$  is the relative speed between the excited oxygen and the  $i$ th species ( $\text{SO}_2$ ,  $\text{SO}$ ,  $\text{O}_2$ ,  $\text{S}$ , and  $\text{O}$ ). The relative speed,  $v_{o^*-i}$ , is assumed to be the most probable relative speed given the excited oxygen's velocity and the local temperature of the gas. A collision occurs (and the excited oxygen given a new velocity) if  $P_c$  is greater than a random number.

Collisions with a neutral de-excite (quench) the excited O atom with a probability  $P_{\text{Quench}}$ . While the quenching probability is, in general, a function of (at least) the identity of the collision partner and the relative velocity between the two particles, here we assume that  $P_{\text{Quench}}$  is constant and independent of species type. Clark and Noxon (1972) generated excited  $\text{O}(\text{¹D})$  via photolysis of  $\text{O}_2$  and found that the quenching probability was unity for collisions with  $\text{CO}_2$ , 0.55 for  $\text{O}_2$ , 0.45 for  $\text{N}_2$ , and 0.2 for  $\text{CO}$ . Therefore it is reasonable to assume that the quenching probability for collisions with molecules ranges from 0.1 to 1.0 and a constant value of 0.5 is used for the base simulation case.  $P_{\text{Quench}}$  is unknown for collisions of  $\text{O}(\text{¹D})$  with O or S atoms and we have assumed that they quench with the same probability as the molecules. One might expect that the atomic quenching probability would be significantly less than the molecular quenching probability because atomic quenching of the excited state requires the formation of a transient molecule that then transfers the electronic energy into kinetic energy. To test the sensitivity of the simulated emission to the atomic quenching probability,  $P_{\text{Quench}}$  for O and S atoms was set to zero. The emission as viewed from Earth was found to change very little. This is because less than 10% (on the dayside) of the  $\text{O}(\text{¹D})$  collision rate is due to collisions with O or S atoms and hence setting  $P_{\text{Quench}}$  to zero reduces the quenching rate by 10% and increases the mean-time between quenching collisions by a factor of 1.11. This small increase in the quenching lifetime does not appreciably change the region of the atmosphere that can effectively emit  $\text{O}(\text{¹D})$  before being quenched.

If the excited oxygen was not quenched on a given timestep, then we check if it emits spontaneously. The excited oxygen transition (decay) can proceed to three different states ( $\text{¹D}_2 \rightarrow \text{³P}_2$  for 6300 Å,  $\text{¹D}_2 \rightarrow \text{³P}_1$  for 6364 Å, and  $\text{¹D}_2 \rightarrow \text{³P}_0$  for 6392 Å), each of which has a different Einstein-A coefficient,  $A_\lambda$ :  $A_{6300} = 5.63 \times 10^{-3} \text{ s}^{-1}$ ,  $A_{6364} = 1.82 \times 10^{-3} \text{ s}^{-1}$ , and  $A_{6392} = 1.1 \times 10^{-6} \text{ s}^{-1}$  (Rachenko et al., 2008; Sharpee and Slanger, 2006). The probability that an excited oxygen spontaneously decays in a given timestep is given by

$$P_E = 1 - \exp\left(-\Delta t \sum A_\lambda\right) \quad (15)$$

and an [OI] emission event is simulated if the emission probability (Eq. (15)),  $P_E$ , is greater than a randomly generated number. If an excited oxygen spontaneously decays via radiative emission, then the probability of emission at a given wavelength,  $\lambda$ , is equal to

$$P_{E,\lambda} = \frac{A_\lambda}{\sum A_\lambda} \quad (16)$$

Notice that the emission branching ratio (Eq. (16)) into the de-excited states (emission wavelengths) is a constant. Therefore, the simulation simply multiplies  $P_{E,\lambda}$  by the total number of [OI] emission events in a given output cell in order to determine the number of photons emitted due to decay into each of the three lower states. One would expect that most excited oxygen atoms created in re-

gions with high neutral density will de-excite through collisions before they emit because of the long lifetime of the  $\text{¹D}$  state (~134 s). As expected, we find that high density regions, such as the sub-solar point and volcanic plumes, look dark at 6300 Å (and 6364 Å, 6392 Å). It should also be noted that we find no appreciable emission at 6392 Å; though this is not unexpected since its lifetime is ~253 h.

### 3. Results and discussion

#### 3.1. Observation

Io was observed in eclipse using HST/WFPC2 on four separate visits during the 1995 and 1997 jovian oppositions as originally reported by Trauger et al. (1997). Two pre-opposition visits in 1997 provided images just after eclipse ingress while post-opposition visits in 1995 and 1997 monitored Io just prior to eclipse egress. These observations were among the most difficult to schedule with HST, as they require specific HST orbits where the spacecraft visibility window for Jupiter/Io overlaps the period when Io is in shadow and well-separated from Jupiter. Io was observed with the Planetary Camera PC1 (0.0455 arcsec per pixel), at a position offset 6 arcsec diagonally from the WFPC2 pyramid apex. By placing Io near the edge of the detector and choosing the proper telescope orientation, it was possible to keep the image of Jupiter completely within Wide Field Camera 3 (WF3) during all of the exposures. This prevented any detector saturation effects from compromising the PC1 observations, and significantly reduced the brightness of scattered light near eclipsed Io.

Approximately 30 min of science observations were obtained during each visit while HST tracked Io; a log of the observations is presented in Table 4. The results for the F631N observations are listed in Table 5. To allow calibration of the images in jovian coordinates, each visit began and ended with unsaturated images of Jupiter in the WF3 camera. Narrowband filters were employed to isolate specific emission features: F673N admits the [SII] doublet at 6716 and 6731 Å; F631N only admits the [OI] 6300 Å line (and rejects the 6364 Å and 6392 Å lines); and F588N admits the Sodium D lines. Multiple exposures were taken in order to reject cosmic rays, and to guard against possible timing errors in the start of the exposure sequence. Sodium D observations were taken just after ingress or just before egress with the intention of observing Io's sunlit sodium corona near the darkened disk of Io. However, this was not seen. In addition, no emission was detected near Io in the F673N filter at any of the four epochs. The corresponding upper limit for [SII] emission (6716 Å and 6731 Å) near Io is ~5 kR.

For the data analysis, the images were bias-subtracted and flat-fielded. The PC1 images showed a strong background radial brightness gradient in the direction toward/away from Jupiter which was largely removed using a two-dimensional high-pass filter. This subtraction was imperfect, however, leaving behind a residual brightness gradient of ~5 kR across the image field of view as seen in Fig. 6. Cosmic rays were removed by comparing image pairs, and rejecting large positive outliers. Flux calibration was done for all of the above exposure times following the WFPC2 Instrument Handbook (Heyer and Biretta, 2004); for a CCD gain of 7 e/DN, PC1 pixel scale, and a 5.1 AU geocentric distance, the conversion factor is: 1 kR = 1.21 DN. The position of Io in the images was established using images taken just before eclipse ingress, or just after egress, along with the assumption that HST accurately tracked Io's motion in the following/preceding 30 min. The orientation of Io north was derived from HST pointing information and the JPL Horizons database. The System III longitudes of Io and sub-Earth coordinates were derived using JPL's Navigation Ancillary Information Facility (NAIF) subroutines.

**Table 4**

WFPC2 observations of Io during eclipse.

Image name	UT date (start time)	Filter	$T_{\text{exposure}}$ (s)	Comments
u2r60501t1	July 28 1995	F673N	0.5	In eclipse
u2r60502t1	July 28 1995	F673N	230	In eclipse
u2r60503t1	July 28 1995	F673N	230	In eclipse
u2r60504t1	July 28 1995	F673N	230	In eclipse
u2r60505t1	July 28 1995	F673N	230	In eclipse
u2r60506t1	July 28 1995	F673N	230	In eclipse
u2r60507t1	July 28 1995	F673N	0.5	Exiting shadow
u3wh0201 m1	May 17 1997	F588N	0.5	Illuminated
u3wh0202m1	May 17 1997	F588N	260	Entering shadow
<b>u3wh0203m1</b>	<b>May 17 1997</b>	<b>F631N</b>	<b>260</b>	<b>In eclipse</b>
<b>u3wh0204m1</b>	<b>May 17 1997</b>	<b>F631N</b>	<b>260</b>	<b>In eclipse</b>
u3wh0205 m1	May 17 1997	F631N	260	In eclipse
u3wh0206 m1	May 17 1997	F673N	260	In eclipse
u3wh0207 m1	May 17 1997	F673N	0.5	In eclipse
u3wh0101 m1	May 22 1997	F588N	0.5	Illuminated
u3wh0102m1	May 22 1997	F588N	260	Entering shadow
<b>u3wh0103m1</b>	<b>May 22 1997</b>	<b>F631N</b>	<b>260</b>	<b>In eclipse</b>
<b>u3wh0104m1</b>	<b>May 22 1997</b>	<b>F631N</b>	<b>260</b>	<b>In eclipse</b>
u3wh0105 m1	May 22 1997	F673N	260	In eclipse
u3wh0106 m1	May 22 1997	F673N	0.5	In eclipse
u3wh030lr1	October 25 1997	F673N	0.5	In eclipse
u3wh0302r1	October 25 1997	F673N	260	In eclipse
u3wh0303r1	October 25 1997	F631N	260	In eclipse
u3wh0304r1	October 25 1997	F631N	260	In eclipse
u3wh0305r1	October 25 1997	F631N	260	In eclipse
u3wh0306r1	October 25 1997	F588N	260	Exiting shadow
u3wh0307r1	October 25 1997	F631N	0.5	Exiting shadow

Bold text indicates the observations used to generate the composite image.

**Table 5**

Io's position in the torus during observations.

Image name	$\lambda_{\text{III}}$ ( $^{\circ}$ ) <sup>a</sup>	$\Psi_{\text{III}}$ ( $^{\circ}$ ) <sup>b</sup>	$Z_c$ <sup>c</sup>
u3wh0103m1	63.069	-0.0240	-20.76
u3wh0104m1	65.849	-0.0241	-20.16
u3wh0203m1	121.383	-0.0241	3.61
u3wh0204m1	124.163	-0.0241	5.15
u3wh0205m1	126.943	-0.0241	6.69
u3wh0303r1	320.389	-0.0142	-13.07
u3wh0304r1	323.164	-0.0139	-13.87
u3wh0305r1	325.939	-0.0136	-14.64

<sup>a</sup> Jovian system III (magnetic) longitude.<sup>b</sup> Jovian system III latitude (calculated with the O<sub>4</sub> offset tilted dipole magnetic field model, Acuña et al. (1983)).<sup>c</sup> Io's distance from torus centrifugal equator (positive above the equator) in units of  $R_{\text{Io}}$  (see Fig. 8).

The two observations of [OI] 6300 Å emission upon ingress are shown in Fig. 6. The May 17, 1997 observation is shown in Fig. 6a. A bright wake spot is seen shifted to the north by  $\sim 5^{\circ}$  that extends  $\sim 700$  km beyond the limb and has a peak intensity ( $\sim 21$  kR) at an altitude of  $\sim 120$  km above the limb. The upstream/wake spot brightness ratio is  $\sim 0.32$  (though this is most likely too low due to the previously discussed brightness gradient) and a southern limb glow roughly twice as bright as the northern limb glow is seen. In Fig. 6b (May 22, 1997 observation), the bright wake spot is seen to be shifted to the north by  $\sim 29^{\circ}$ , extend to  $\sim 400$  km, and have a peak intensity ( $\sim 18$  kR)  $\sim 90$  km above the limb. For the May 22 observation, the upstream/wake spot brightness ratio is  $\sim 0.44$  and a northern limb glow  $\sim 2.5$  times brighter than the southern limb glow is seen. Equatorial spots are seen in both observations extending across Io from the wake and fading toward the upstream.

### 3.1.1. 1-D [SII] and [OI] calculation results

A one-dimensional Excitation and Emission Model was used to compare the emission intensity from [OI] and [SII]. The vertical S<sup>+</sup>

density profile simulated by Kumar (1985) is used in the 1-D code in addition to the standard atmospheric model described in Section 2.2, and the electron-neutral cross sections in Section 2.3.3. Such a model is comparable to the 1-D model by Bhardwaj and Michael (1999b) and Michael and Bhardwaj (2000a,b) with the exception that we calculate the emission intensity of a specific line, as opposed to calculating yield spectra (Singhal and Haider, 1984) and can include the magnetic field. Electrons from the plasma torus are input continuously and, once steady state is reached, a time-averaged emission rate for [SII] and [OI] is obtained.

We use the one-dimensional simulation to examine the relative [SII] emission from sulfur ions at 6716 Å and 6731 Å ( $A_{6716} = 4.7 \times 10^{-4} \text{ s}^{-1}$  and  $A_{6731} = 4.3 \times 10^{-4} \text{ s}^{-1}$ , Ralchenko et al., 2008) to [OI] 6300 Å emission. The electron-S<sup>+</sup> excitation cross section for [SII] is not known; hence as a crude approximation for the excitation cross section we took the [OI] excitation cross section, shifted the threshold energy from 1.96 eV to 2.1 eV, and then scaled the cross section parametrically by a constant,  $\gamma$ , in order to compare the resultant [SII] emission with the [OI] 6300 Å emission. In Fig. 7, we see that [SII] emission is significantly weaker than [OI] 6300 Å emission even if the electron excitation cross section were as much as three orders of magnitude larger than the [OI] excitation cross section (which is unlikely). Therefore, we know that if the cross section were small, then the [SII] emission intensity would be much lower than the [OI] intensity. However, even if the excitation cross section were un-physically large, the [SII] emission would be relatively dim due to two additional factors. First, the S<sup>+</sup> density is more than two orders of magnitude lower than the O density which directly influences the possible emission intensity through the number of [SII] excitation events. Also, the Einstein-A coefficient for [SII] emission is  $\sim 10$  times smaller than the Einstein-A coefficient for [OI] emission. A small Einstein-A coefficient allows for increased collisional quenching due to the state's increased lifetime and therefore reduces the fraction of excited sulfur ions that spontaneously emit. Consequently the peak emission from excited sulfur ions occurs at lower total gas

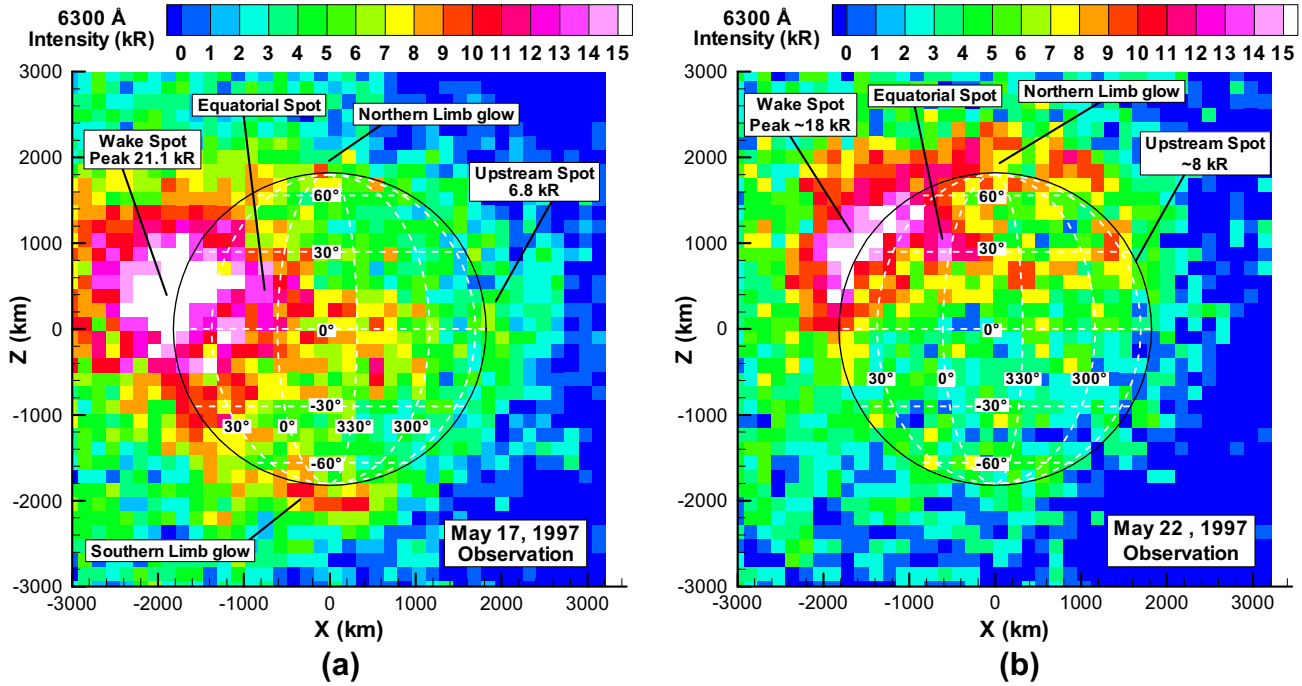


**Fig. 6.** Observations of [OI] 6300 Å emission from Io in eclipse. Average of two 260 s exposures taken by Trauger et al. (1997) with WFPC2. (Table 4). (a) Taken on May 17, 1997 starting at 06:39:14. (b) Taken on May 22, 1997 starting at 14:04.

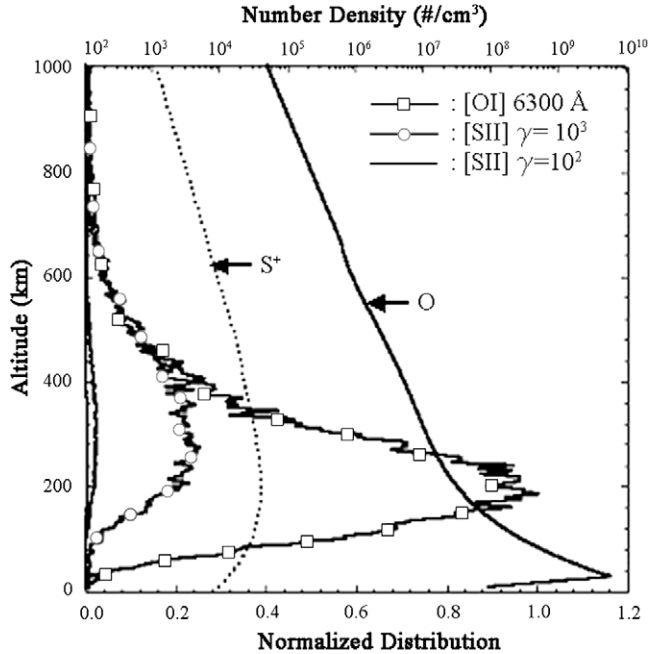


**Fig. 7.** The [OI] 6300 Å and [SII] 6716 Å and 6731 Å emission. We normalize the emission intensity by the peak value of [OI] at  $\sim 200$  km.  $\gamma$  is the ratio of excitation cross section of [SII] 6716 Å and 6731 Å to that of [OI]. Even when  $\gamma = 100$  (circles), the emission intensity is still small.  $S^+$  and  $O$  number densities ( $\text{cm}^{-3}$ ) are also shown.

densities (higher altitudes) than for [OI] emission. The [SII] emission is seen to peak at  $\sim 300$  km, roughly 100 km higher than the simulated [OI] peak emission, primarily because of the difference in the two Einstein-A coefficients.

Alternate production paths for [SII] emission such as ionization-excitation of  $\text{SO}_2$  (or  $S$ ) were briefly considered. While the ratio of  $\text{SO}_2$  to  $S^+$  density is  $\sim 10^4$  above 200 km where collisional

quenching is negligible, there are 14 times more thermal electrons with sufficient energy (2.1 eV) to excite  $S^+$  directly than to ionize and excite  $\text{SO}_2$  (18.6 eV). Similarly there are significantly more  $S$  atoms than ions, but fewer thermal electrons are capable of ionization-excitation. Therefore the emission due to  $\text{SO}_2$  and  $S$  may exceed emission due to direct excitation of  $S^+$ , though the ionization-excitation cross sections are unknown. In each case, the excitation cross section was assumed to be a constant fraction,  $\delta$ , of the respective ionization cross section to  $S^+$  with the threshold energy shifted by 2.1 eV to account for the excitation energy. Even if every ionization event above threshold produced [SII] ( $\delta = 1$ ), the simulated emission produced from these other production paths was less than 0.2 kR, or  $\sim 2\%$  of the [OI] 6300 Å emission intensity. Therefore, the [SII] emission intensity from ionization-excitation of  $\text{SO}_2$  and  $S$  is roughly equivalent to the intensity due to  $S^+$  excitation if  $\gamma = 100$ . Therefore, even if ionization-excitation of  $\text{SO}_2$  (or  $S$ ) is the dominant excitation mechanism (e.g.  $\gamma \ll 100$ ,  $\delta \sim 1$ ), it would still produce negligible [SII] emission relative to [OI] emission. [SII] emission from ionization-excitation of  $S_2$  present in the plumes was not simulated in this model, though the densities present in the plumes should quench virtually all of the resultant emission. These results suggest that Trauger et al.'s (1997) lack of detectable [SII] emission is consistent with reasonable excitation cross sections and densities found on Io.

Fig. 8 shows the emission profile with inclusion of a single volcanic plume (Pele) and the magnetic field (Section 2.3.1). Instead of doing a 1-D simulation along a simple radial line out of the planet center, the thermal electrons travel normal to the equatorial plane along the line tangent to Io's surface and perpendicular to the plasma flow, as shown in the inset in Fig. 8. Also note that the atmospheric density profiles (other than Pele) used were identical upstream and in the wake in order to isolate the effects of Pele and the magnetic field. The solid line without symbols corresponds to the emission profile in the wake ( $X = -1900$  km), and the lines with circles and squares are the profiles on the upstream side ( $X = 1900$  km). Note that for the sake of comparison the simulation does not account for the flux tube depletion. An incoming electron

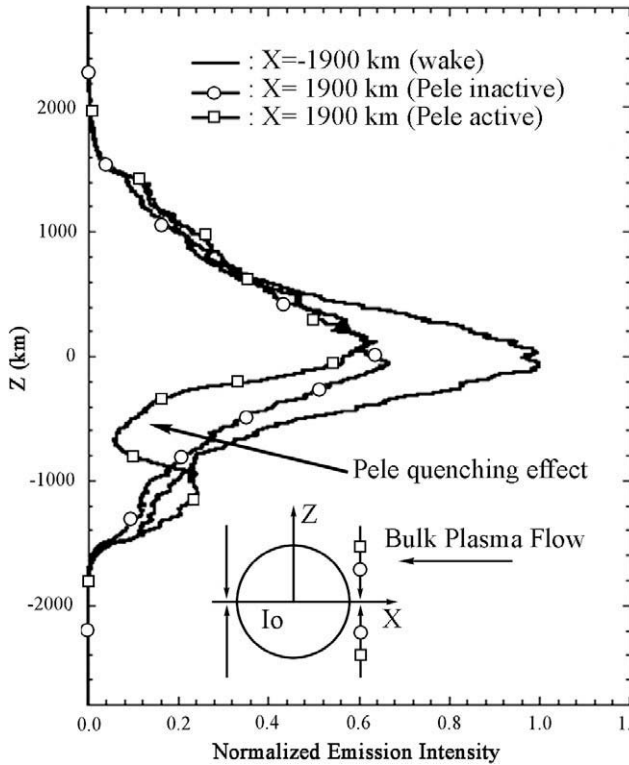


**Fig. 8.** Upstream and wake [OI] 6300 Å emission profiles for a 1-D simulation what considers a single active plume (Pele) and the perturbed magnetic field. Three cases are shown: one (no symbols) represents the wake region and the others (circles and squares) are for the upstream region. As shown in the corner schematic, the Z-axis is perpendicular to the plasma flow and Io's equatorial plane. We normalize the emission intensity by the value of the wake emission at the equator ( $Z = 0$  km). In order to check the quenching effect of Pele, we calculate the intensity in two cases where Pele is active (square symbols), and where Pele is dormant (circles). Similarly, the mirror effect is examined by comparing the wake emission (no symbols) to the upstream emission without Pele (circles).

on the upstream side encounters an increasing magnetic field and the dense atmosphere of Pele's plume. On the other hand, in the wake, the magnetic field decreases and the atmosphere is not enhanced by Pele. To quantify the quenching effect of Pele, we calculated the intensity of upstream emission when Pele is active (squares) for comparison to the case when Pele is dormant (circles). We see that Pele quenches the emission strongly around  $Z = -600$  km and actually increases the emission around  $Z = -1200$  km. Both effects occur because many electrons entering from the south are backscattered by the plume (or produce low-energy secondaries). Therefore, fewer electrons penetrate into the plume and the excitation rate of [OI] at the edge of Pele is increased. Furthermore, by comparing the peak wake emission to the peak upstream emission without Pele, one sees that the magnetic mirror effect reduces the upstream intensity by ~40%. The mirror effect and, to a much lesser extent, Pele's quenching effect are important contributors to the reduced overall upstream [OI] intensity. However, note that the magnitude of the intensity reduction due to the mirror effect is controlled by the magnitude of the upstream magnetic field perturbation and the pitch angle distribution of the electrons.

### 3.1.2. 3-D simulations

The bright spot in the plasma wake (its intensity, altitude, and longitude on Io), the much smaller and dimmer upstream emission, the limb glow, the diffuse coronal emission, and the lack of bright plumes are the key features to be explained in the eclipse in-

gress images of [OI] 6300 Å emission. For the simulations, Io's latitude in the torus and the jovian magnetic field orientation at Io's location was computed using the O<sub>4</sub> offset tilted dipole magnetic field model (Acuña et al., 1983). Our simulated absolute emission intensity is directly proportional to the upstream electron density because the electron number flux is proportional to the upstream electron density and the model's magnetic field and atmospheric profiles are unchanged by upstream electron density changes. The lack of significant [SII] emission (and plume emission) was explained with the 1-D emission simulations, and so no 3-D [SII] emission simulations will be presented here. Explaining the presence of a bright wake feature shifted latitudinally off Io's equator and the lack of a corresponding upstream feature is crucial. First, a base case that best matches the observations will be shown, then several parameters will be varied to show how they affect the emission around Io. For all the results presented here, each case was simulated 10 times with different random number seeds. The sampled properties (e.g. 6300 Å intensity) were then ensemble averaged to give the plotted results. The Monte Carlo error was estimated assuming that our results were sampled from a normal distribution. For all the results shown, the error was less than 6% below 600 km altitude except in the vicinity of Pele, where it was up to ~10%.

### 3.1.3. Base case

Base case simulations are presented in Fig. 9a–d which provide the best match to the observations shown in Fig. 6a and b. In Fig. 9a and b the original simulation results (Fig. 9c and d) have been binned into the observation's coarser grid and convolved with observation-specific point spread functions. These were generated using the publically available Tiny Tim software developed at the Space Telescope Science Institute to replicate their instrumental point spread functions. Io's position in the torus and the upstream magnetic field orientation are set to the corresponding values at the time of the two observations (Table 5) and the plumes (Table 1) are all active except Tvashtar and Dazhbog. The sublimation SO<sub>2</sub> density across the dayside was scaled by the ratio of the column density for  $T_{SS} = 115$  K to the column density for  $T_{SS} = 120$  K (Eq. (3)) and by the partial collapse factor as discussed above (Section 2.2.1). The probability of quenching was assumed to be 0.5 for collisions with all neutral species. Finally, the upstream temperature of the thermal electrons was 5 eV, the electrons were assumed to re-thermalize with the plasma torus if they left the domain and returned, and their pitch angle was assumed to be isotropic far from Io (and then perturbed by the local magnetic field at the edge of the domain).

In this case, the emission morphology, including the wake spot and upstream brightness agrees with the observations reasonably well, though the peak [OI] 6300 Å wake spot intensity in the convolved simulation results (Fig. 9a and b) is off by a factor of ~3 compared to the observations in Fig. 6a and b. Though not shown, simulations with Io above the torus equator yield similarly intense wake spots which are a factor of ~1.5 less than Rutherford's (2002) observed [OI] 6300 Å wake spot intensity when Io was above the torus equator ( $Z_c = 15.9$ ).

For Fig. 9a, the upstream/downstream brightness ratio (defined as the ratio of the peaks) is 0.68 while the observed ratio (Fig. 6a) is ~0.32. For Fig. 9b the upstream/downstream brightness ratio is ~0.73 compared to the observed ratio (Fig. 6b) of 0.44. For comparison, Rutherford's observations showed an upstream/downstream brightness ratio of ~0.36. While the simulation results have higher upstream/downstream brightness ratios than the observations, the processed observation images (in Fig. 6) still contain a residual brightness gradient across Io that likely acts to reduce the observed upstream/downstream brightness ratio. The latitudinal location of the simulated peak wake emission (~30°N, Fig. 9b) agrees well

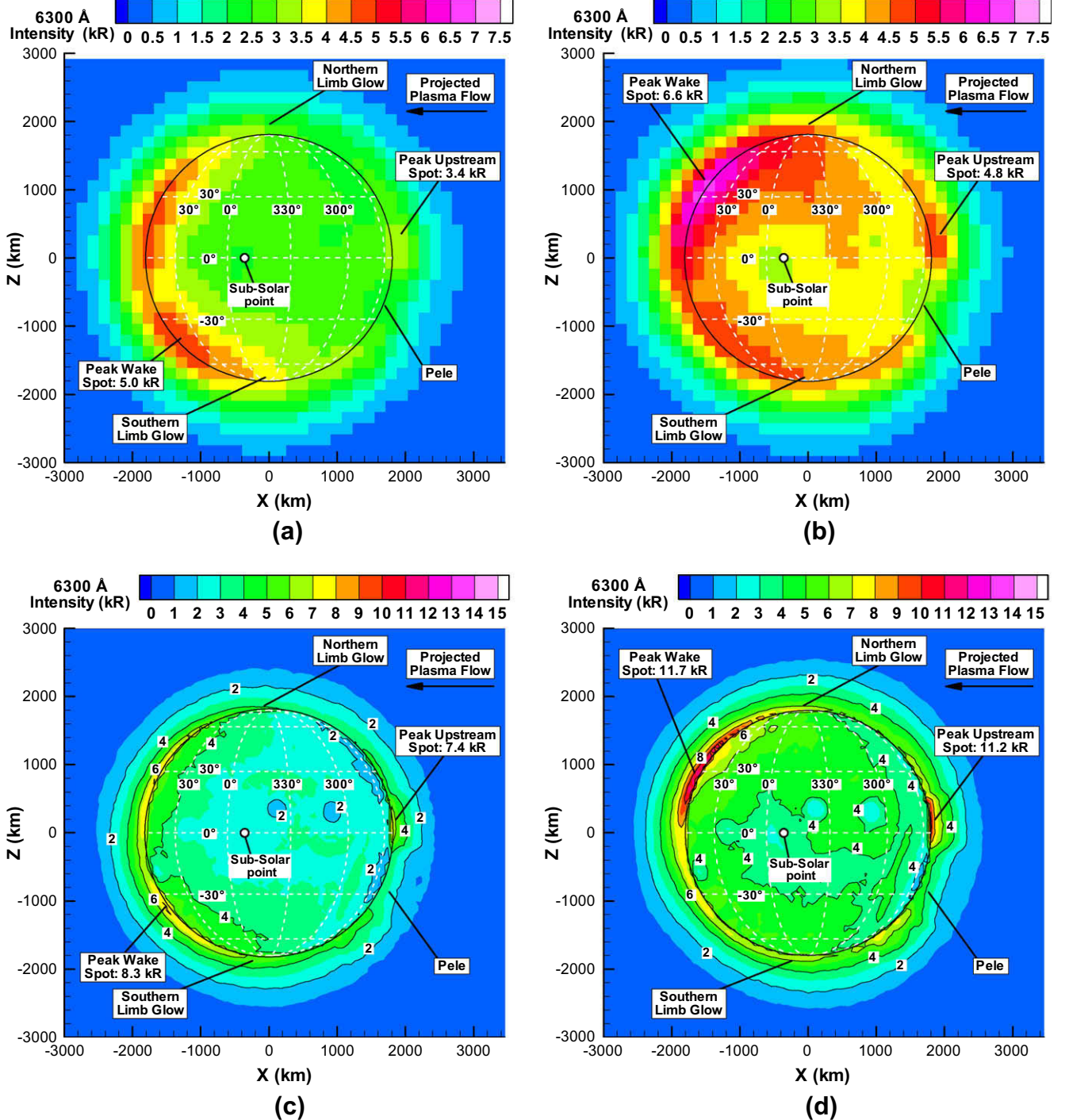


**Fig. 9.** The simulated line of sight [OI] 6300 Å emission profiles (viewed from Earth, the upstream plasma comes roughly from the right). Shown are (a) the convolved May 17 simulation results, (b) the convolved May 22 simulation results, (c) the un-convolved May 17 data, and (d) the un-convolved May 22 data. Note that the colorbar for (a) and (b) is from 0 to 7.5 kR in order to bring out details in the emission contours. Several circular regions of low intensity are due to (from left to right) the quenching effect of the plumes Kanehiki, Grian, Acala, Loki, and Pele. The thick solid black line shows Io's surface, the thinner black lines are contours every 2 kR, and the white dashed lines show lines of latitude and longitude.

with the May 22 observation ( $\sim 29^{\circ}\text{N}$ , Fig. 6b). The emission extends across Io and reproduces the morphology of the observation reasonably well given the level of approximation used in generating the sublimation atmosphere. The morphology of the simulated emission on May 17 (Fig. 9a) does not agree well with the observation (Fig. 6a). The observed peak wake emission occurs at  $\sim 5^{\circ}\text{N}$  and extends over  $\sim 30^{\circ}$  latitude whereas the simulated peak wake emission straddles the equator. Future work will investigate possi-

ble causes for the discrepancy between the simulated and observed May 17 emission. Furthermore, the simulation results do not seem to have as prominent an equatorial spot (which we could approximately match only if we further reduced the atmospheric density across Io). The altitude of the simulated peak emission ( $\sim 25$  km, essentially on the limb) is lower than the observed peak emission at  $\sim 100$  km. Also, the simulated wake spot brightness above Io's limb falls off with altitude faster than observed. The sim-

ulated northern limb glow is slightly more intense than the southern limb glow; however, the ratio of north/south limb glow emission does not agree well with observations (Retherford et al., 2003). Finally, the simulated coronal emission is much dimmer than observed, again possibly due to incomplete subtraction of scattered light from Jupiter in the observations.

Fig. 9c and d shows the simulated emission un-convolved on the original fine simulation grid. The wake emission is now only slightly brighter than the upstream emission, with an upstream/downstream ratio of  $\sim 0.89$  (Fig. 9c) and  $\sim 0.96$  (Fig. 9d). Also, in the un-convolved images several volcanic plumes on the dayside can be seen as dim circles where emission is largely quenched due to the high densities in the plumes. Upstream, Pele is seen to locally dim the limb in the southern hemisphere. The remaining simulation emission images will be shown un-convolved so that smaller changes can be seen when changing various parameters.

Average radial emission profiles (from upstream of Io and into the wake) were computed from both the simulation and the observation data following Retherford's (2002) method as illustrated in the inset schematic of Fig. 10. The emission intensity at a given distance,  $R$ , from the center of Io (the sub-Earth point in our images) is computed by averaging pixels within  $90^\circ$  arcs ( $0.05R_{Io}$  wide) centered on Io's equator. Note that the emission is only radially averaged from  $0.2R_{Io}$  to  $1.7R_{Io}$ . Fig. 10 shows data from the May 22, 1997 observation, an August 27, 1999 observation (Retherford, 2002), the base case, the convolved base case, and a case showing the effect of our atmospheric scaling (Section 2.2.1). The overall agreement with the observation is decent; the May 22 convolved base simulation's upstream emission intensity agrees very well with both observations and the simulated emission across Io's disk agrees well upstream but is somewhat too low towards the wake. The result is that the convolved simulation's wake spot intensity (radially averaged) is too dim by a factor of  $\sim 1.8$ . This behavior across Io's disk and into the wake could be interpreted as an error in the model for the flux tube depletion across Io, i.e. it is too large.

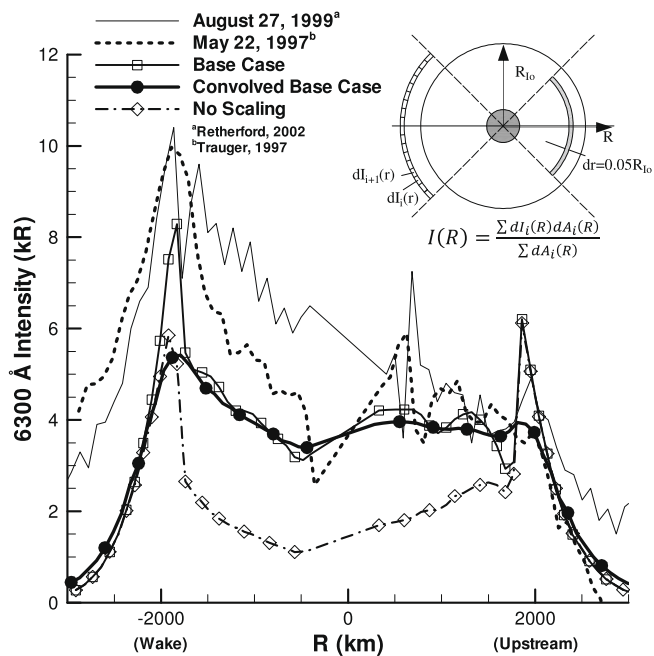


**Fig. 10.** Radial brightness profiles (see schematic inset, note that the  $R$ -axis is in the direction of Fig. 9's  $X$ -axis) of  $[OI]$  6300 Å emission for May 22, 1997 observations and simulations. To show that the observed radial profiles are largely independent of Io's position in the torus, Retherford's (2002) data for August 27, 1999 when Io is above the torus equator ( $Z_c = 15.9$ ) is shown. The wake is shown for negative values of  $R$ .

However, if the flux tube depletion across Io is neglected (see Moore et al., 2004), then the simulated wake spot is more intense, but the latitudinal position is not in agreement with the observations. Another possibility for the low wake emission is that we are neglecting dissociative-excitation from  $SO_2$  as a source of excited O and that the current simulated upstream intensity is larger than it should be for direct O excitation. This could be because our model does not account for the compression of the upstream atmosphere (increasing quenching) due to plasma impingement (Saur et al., 2002) and the field model might under-predict the compression of magnetic field upstream which would increase mirroring and reduce the electron flux to the upstream region.

In Fig. 10, the peak simulated emission altitude above the limb of Io is seen to be lower than the peak of the observed emission altitude. In addition, above the limb the simulated emission intensity falls off with altitude faster than observed, both upstream and in the wake (assuming Retherford's data are more accurate because there is a smaller brightness gradient across Io). The falloff is insensitive to the quenching probability because above  $\sim 100$  km, effectively no quenching occurs and hence all excited O atoms are already spontaneously emitting for nominal values of  $P_{Quench}$ . Also, the rate of falloff is unaffected whether or not the atmosphere is scaled due to partial collapse during eclipse because above  $\sim 100$  km the atmospheric density does not collapse early in eclipse (Moore et al., 2009). Furthermore, though not shown, the falloff in intensity above the limb is not affected by the upstream electron temperature or the presence of volcanoes. In Fig. 10, the un-convolved base case is seen to have sharper peaks on the limb of Io and decrease slightly faster away from the limb in comparison to the convolved case, as one would expect. Finally, note that the simulated radial (un-convolved) emission curve with no atmospheric scaling (both eclipse scaling and sub-solar temperature scaling (Eq. (3)) turned off) is much dimmer than the base case in the wake and across Io.

The differences between the simulated and observed emission (absolute intensity, upstream/wake spot intensity ratio, altitude of peak wake emission, emission intensity across Io, north/south limb glows) arise from several factors. The various model assumptions/simplifications that are the most likely cause of significant differences with the observations will be discussed below, as will the results of sensitivity analysis for some of the parameters. Also, note that much of the inconsistency and, perhaps, error related to our atmospheric model will be corrected in a future paper that incorporates a 3-D DSMC simulation of Io's rarefied sublimation atmosphere after ingress into eclipse. The DSMC model is currently under development and will include an inhomogeneous frost map distribution, a two temperature model for the surface that accounts for Io's rotation (Walker et al., 2010; Gratiy et al., 2010), and ion, electron, and photo-chemistry.

The simulated emission intensity should be sensitive to the quenching probability since  $\sim 65\%$  of the excited oxygen atoms are quenched in the base case simulation. However, the probability that the excited oxygen de-excites (quenches) upon collision with a neutral is not known precisely, and we have assumed a constant value of 0.5, though values ranging from 0.1 to 1.0 are reasonable for  $O(^1D)$  collisions with molecules (Clark and Noxon, 1972). Fig. 11 shows the emission intensity if the quenching probability is reduced by a factor of five ( $P_{Quench} = 0.1$ ). The overall emission intensity is seen to increase, though the plumes are still seen to be dim. Notice that the wake spot broadens and brightens more than the upstream spot. Decreasing the quenching probability by a factor of five caused the simulated wake spot brightness to increase by a factor of  $\sim 1.8$ . Also, as expected, the altitude at which the emission peaks is sensitive to the quenching probability since lower probabilities allow emission to occur at higher neutral densities closer to the surface. A related result is that the upstream/

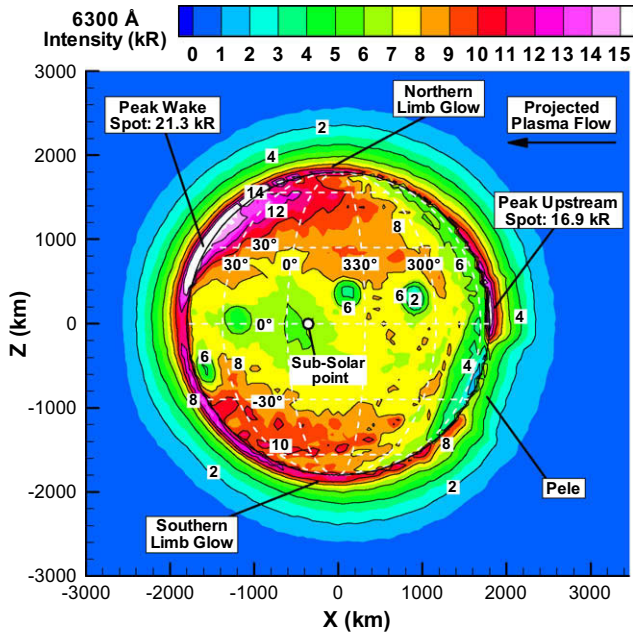


**Fig. 11.** Simulated [OI] 6300 Å emission for May 22, 1997 assuming  $P_{Quench} = 0.1$ . The plumes are still relatively dim, but the intensity upstream and in the wake is seen to increase, respectively, 51% and 82% as compared to the base case (Fig. 9d).

wake spot intensity ratio decreases (to 0.79 for  $P_{Quench} = 0.1$ ) for smaller quenching probabilities because the wake viewing geometry from Earth looks partially across the dense dayside atmosphere whereas the upstream viewing geometry looks partially across the nightside atmosphere. If  $P_{Quench}$  is increased to unity, then the peak wake intensity becomes roughly equal to the upstream spot and the overall emission decreases correspondingly.

As discussed earlier, the model lacks direct reaction paths from SO<sub>2</sub> and SO to O(<sup>1</sup>D) since no electron impact dissociation-excitation cross sections are available. However, there is suggestive evidence that substantial emission occurs from oxygen excited via dissociation-excitation (Oliversen et al., 2001) and therefore our simulated intensity should be less than the observed intensity. In addition to increasing the overall emission intensity, one might expect the addition of this excitation pathway to decrease the upstream/wake spot intensity ratio because the wake line of sight intersects the larger dayside SO<sub>2</sub> column as opposed to the upstream line of sight which intersects the much lower nightside SO<sub>2</sub> column. Finally, inclusion of direct dissociative-excitation of SO<sub>2</sub> to O(<sup>1</sup>D) should preferentially increase the excitation rate in the equatorial regions where the SO<sub>2</sub> column density is highest (Strobel and Wolven, 2001; Jessup et al., 2004; Feaga et al., 2009) which may be one reason the May 17 simulated emission does not agree with the observations.

Another error source is the atmospheric model used in the simulation. A complete model would simulate an ionian atmosphere that extends up to ~500 km in altitude, includes a longitude/latitude dependence both due to frost coverage and surface temperature distribution, multiple species accounting for chemistry, volcanic plumes, and has time variability during eclipse. The atmospheric profiles used in the present model are the best currently available that self-consistently account for chemistry; however, they are from a continuum simulation (Wong and Smyth, 2000; Smyth and Wong, 2004). Since most of the [OI] 6300 Å emission occurs at high altitudes where the atmosphere is rarefied, the accuracy of the continuum model at typical emission altitudes is questionable. The error in the altitude of the peak wake spot emission and its vertical extent is probably dominated by errors in the ver-

tical neutral profiles, especially O and SO<sub>2</sub> (since the SO<sub>2</sub> dominates quenching). As mentioned previously, Smyth and Wong's (2004) atmosphere, which has a very different altitudinal distribution of species due to inclusion of electron chemistry, was also used. However, it was found to yield [OI] emission intensities that were higher on the upstream side of Io and the intensities were in general much higher than observed when using our curve-fit to their published data. Provided our simulation results would not change substantially given their complete simulated atmospheric profiles, we conclude that the improved atmospheric model contains too much atomic oxygen at high altitudes (or not enough other species for quenching) since our model should tend to under-predict the emission intensity.

There is further possible error in the model atmosphere because the atmospheric profiles assumed a sub-solar temperature of 120 K which more recent evidence suggests is too high (Feaga et al., 2009; Walker et al., 2010). Fig. 12a shows the base case simulation for May 22 with Wong and Smyth's (2000) original atmosphere scaled for collapse during eclipse but without scaling the atmospheric column density down to a sub-solar temperature of 115 K (Eq. (3)). It is seen that the overall intensity decreases and the simulated emission has a pronounced local minimum near the sub-solar point (also seen in the radial emission plot, Fig. 10) that is not observed. Also, the upstream spot is now brighter than the wake such that the upstream/downstream brightness ratio increased to 1.4. It seems that Wong and Smyth's (2000) high density case has SO<sub>2</sub> column densities that are too high whereas their low density case (at  $T_{SS} = 113$  K; not shown) produced much less emission than observed. In addition, the Wong and Smyth (2000) atmospheric profiles are for Io in sunlight. Therefore the partial collapse of the atmosphere due to eclipse, the severity of which varies from the wake ("dawn" terminator) to the upstream ("dusk" terminator) side, is not accounted for by the original simulated atmospheric profiles. As discussed previously, the partial atmospheric collapse is only crudely modeled and inclusion of an atmosphere which directly simulates collapse would reduce errors from the simplified model used to account for collapse. Fig. 12b shows the base case simulation for May 22 without inclusion of partial atmospheric collapse. The upstream spot is seen to be more intense than the wake spot, and the overall emission intensity is slightly weaker when partial collapse is not modeled.

The current atmosphere is adopted from simulations that assume a uniform frost distribution and neglect Io's rotation resulting in an axisymmetric solution for the atmosphere as a function of altitude and SZA. The assumption of uniform frost might lead to densities near the poles that are too high and hence affect the simulated limb glow emission (by changing the quenching rate) and the flux tube depletion across Io (via increased/decreased electron backscatter). Finally, inclusion of Io's rotation and reasonable thermal inertias for the rock and frost into the simulation of the neutral atmosphere lead to a skewed frost surface temperature that lags the sub-solar point by up to 30° towards the dusk terminator (Walker et al., 2010). The frost temperature lag yields a corresponding lag in the peak SO<sub>2</sub> column density and hence the SO<sub>2</sub> column should peak closer to the upstream side of Io leading to increased quenching upstream relative to the wake.

Further possible sources of error in the simulated morphology and upstream/wake spot brightness ratio include errors in (i) the approximate model for flux tube depletion across Io, (ii) the compression of the atmosphere on the upstream side of Io due to the force of the impinging plasma (Saur et al., 2002), (iii) the lack of the Hall effect in our model (Saur et al., 2000), (iv) the percentage of the plasma diverted around Io, (v) the bulk plasma velocity below Io's ionosphere, and (vi) the magnitude of the magnetic field compression upstream of Io. Error in the flux tube depletion and the fraction of plasma diverted around Io primarily effects the

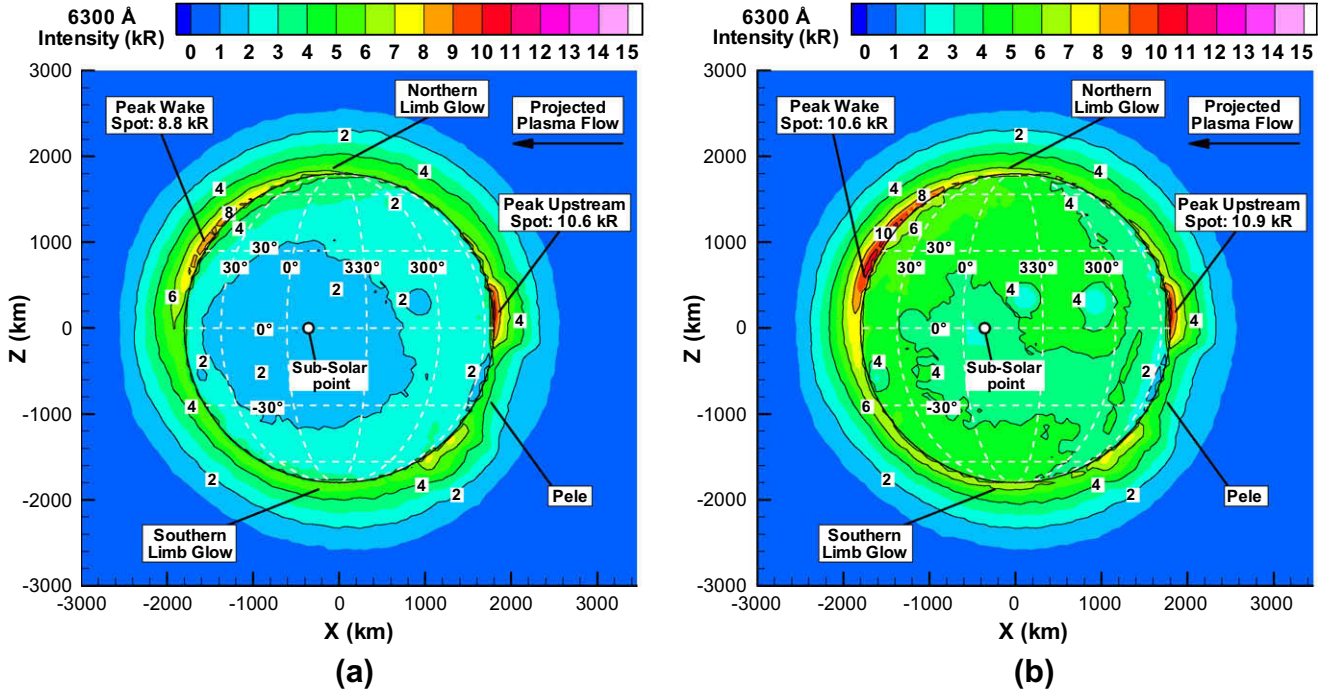


**Fig. 12.** Simulated [OI] 6300 Å emission on May 22 if the SO<sub>2</sub> density is (a) not scaled to correct the column density for a sub-solar temperature of 115 K (Eq. (3)) and (b) not scaled to account for varying partial collapse across Io during eclipse. In (a) the increased SO<sub>2</sub> density, especially near the sub-solar point, results in decreased emission. In (b) the increased SO<sub>2</sub> density on the wake side (relative to the upstream side) results in an increase in the upstream/downstream brightness ratio. Note that simulations with Wong and Smyth's (2000) original (no scaling) atmosphere are not shown since the emission is very similar to (a) except that the wake is ~12% dimmer.

wake spot intensity whereas the upstream intensity is effected by error in the compression of the upstream atmosphere (higher quenching) and magnetic field (reduce the upstream flux of electrons via mirroring). The lack of Hall effect is discussed below. Finally, error in the bulk plasma velocity, especially near the surface in the wake, effects the wake intensity near the equator; simulations of May 17 with an artificial reduction in the wake region's plasma velocity resulted in better agreement with the observation's emission morphology.

Fig. 13a is the north polar view of the aurora and Fig. 13b shows the emission seen from roughly upstream of Io for the base case. Fig. 13a shows that the [OI] emission is brighter on the sub-jovian side than the anti-jovian side. However, the field model used in our simulations does not account for the Hall effect which has been argued to preferentially brighten the anti-jovian side (Saur et al., 2000). In Fig. 13b the sub-Earth spot (roughly the sub-jovian spot) is once again seen to be brighter than the anti-Earth spot and several plumes are again seen as dim regions with little emission.

### 3.1.4. Parametric studies

To better understand the effects of various parameters on the [OI] emission, we now explore several of them parametrically. In order to examine the origin of the wake spot shift, we first artificially set Io's position at the plasma torus equator but keep the proper upstream jovian magnetic field orientation ( $\lambda_{\text{III}} = 64.5^\circ$ ,  $\Psi_{\text{III}} = -0.024^\circ$ ,  $Z_c = 0$ ). Then the upstream jovian magnetic field is oriented as if Io was located at the proper magnetic latitude in the torus but placed at the torus equator ( $\lambda_{\text{III}} = 120^\circ$ ,  $\Psi_{\text{III}} = 0^\circ$ ,  $Z_c = -20.4$ ). To examine the effects of the volcanic plumes on emission, we simulate the emission with Tvashtar and Dazhbog active and also simulate the emission with all the volcanoes dormant. Finally, we examine the sensitivity of the emission to the upstream electron temperature.

Fig. 14a shows the line-of-sight integrated simulation emission column intensity for the far-southern magnetic latitude May 22

observation (Fig. 9d), but with Io located at the torus equator ( $Z_c = 0$ ). It is seen that the wake spot is no longer located at the appropriate latitude on Io and, in fact, the emission across Io looks very similar to the May 17 simulations (Fig. 9c). Fig. 14b shows the simulation line of sight emission intensity with Io properly offset from the torus equator ( $Z_c = -20.4$ ), but with the magnetic field oriented as if Io were actually at the torus equator. The wake spot is now brighter and located at the approximate latitude observed because the electron flux tube depletion across the northern hemisphere decreases due to the increase in the distance to the northern plasma torus edge (therefore decreasing the number of scattering events required to reach the wake). Based on these results, it seems reasonable to conclude that Io's latitude in the torus is an important contributor to the behavior of the wake spot through the asymmetric flux tube depletion across Io as described earlier. However, one cannot conclude from these results that the magnetic field orientation does not affect the wake spot latitude; the field used in our model is not self-consistent because it was computed for a given location in the torus (Combi et al., 1998) and we then rotated the upstream field to match the conditions at the time of our observations.

Fig. 15a shows the emission with Tvashtar and Dazhbog active and all other parameters the same as for the base case (Fig. 9d). Dazhbog is visible as a dim region that extends over the limb in the northern hemisphere on the upstream side of Io. Similarly, even though Tvashtar is on the nightside of Io, its canopy rises above the limb and results in a small region of decreased emission; the effect is limited because the majority of the line-of-sight integrated emission comes from the dayside atmosphere. Also, compared to Fig. 9d, the wake spot in Fig. 15a is slightly brighter and the upstream spot is dimmer though both variances are within the Monte Carlo noise for the simulations. Fig. 15b shows the emission with all the volcanoes dormant. The most striking change in the emission relative to the base case (Fig. 9d) is that, across Io, there are no longer dim regions where several of the smaller

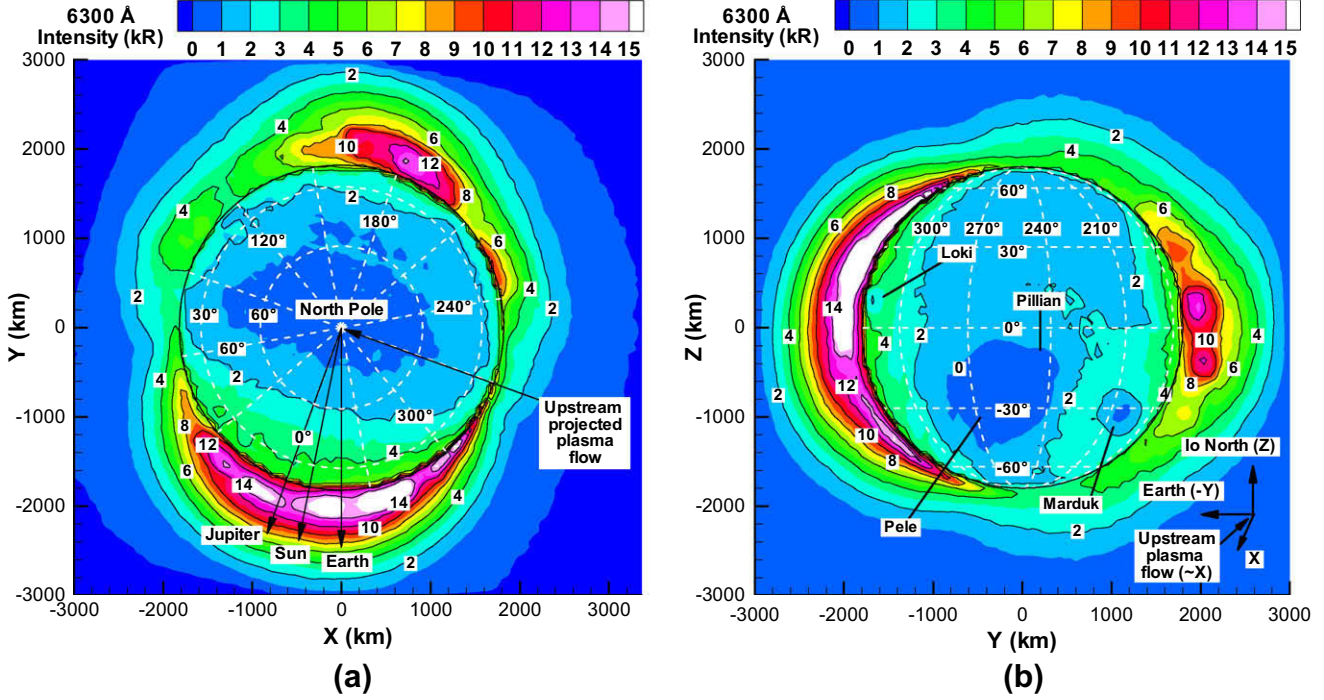


**Fig. 13.** Simulated [OI] 6300 Å line-of-sight integrated emission on May 22 from (a) the north polar view and (b) the upstream view. The emission is seen to be dimmer on the nightside due to the relative lack of oxygen there. The anti-jovian spot is dim relative to the jovian spot; however, our model does not include the Hall effect, which should tend to increase the anti-jovian spot intensity.

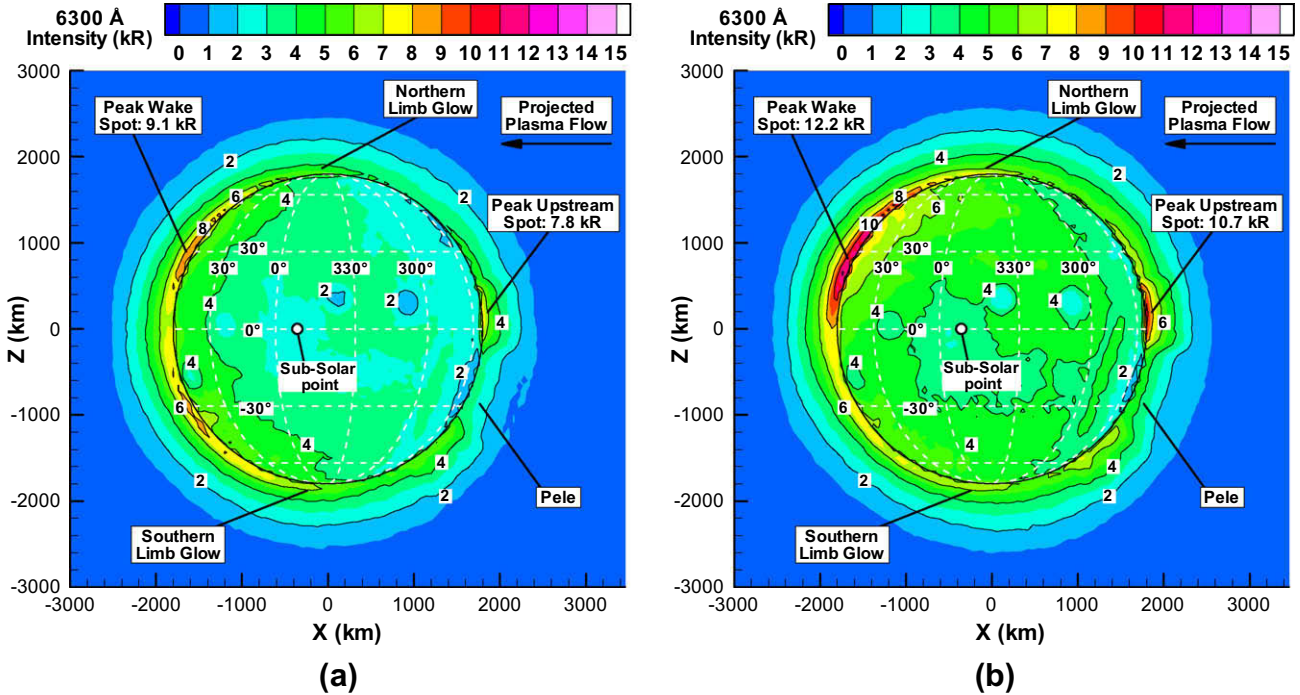


**Fig. 14.** Simulated [OI] 6300 Å emission for May 22 observation (a) with the magnetic field oriented properly, but Io artificially located at the plasma torus equator and (b) with Io properly located in the plasma torus, but with the magnetic field oriented as if Io were at the torus equator. In (a) the wake emission is located about Io's equator whereas in (b) the wake emission is located  $\sim 23^\circ$  above the equator.

plumes existed. The peak wake spot brightness is seen to decrease  $\sim 3\%$  with no active plumes (within the noise) while the peak upstream brightness is seen to decrease  $\sim 30\%$  with all plumes dormant (notably Pele). However, the total, or average, upstream emission remains roughly constant whether the plumes are active

or dormant. When Pele is dormant the upstream emission on the limb is much more uniform between  $\pm 25^\circ$  latitude. As seen in Fig. 8 (and in comparing Figs. 9d and 15b), when Pele is active, the emission increases just outside of Pele. Comparison of Figs. 9d and 15b demonstrates that volcanoes with nominal oxy-

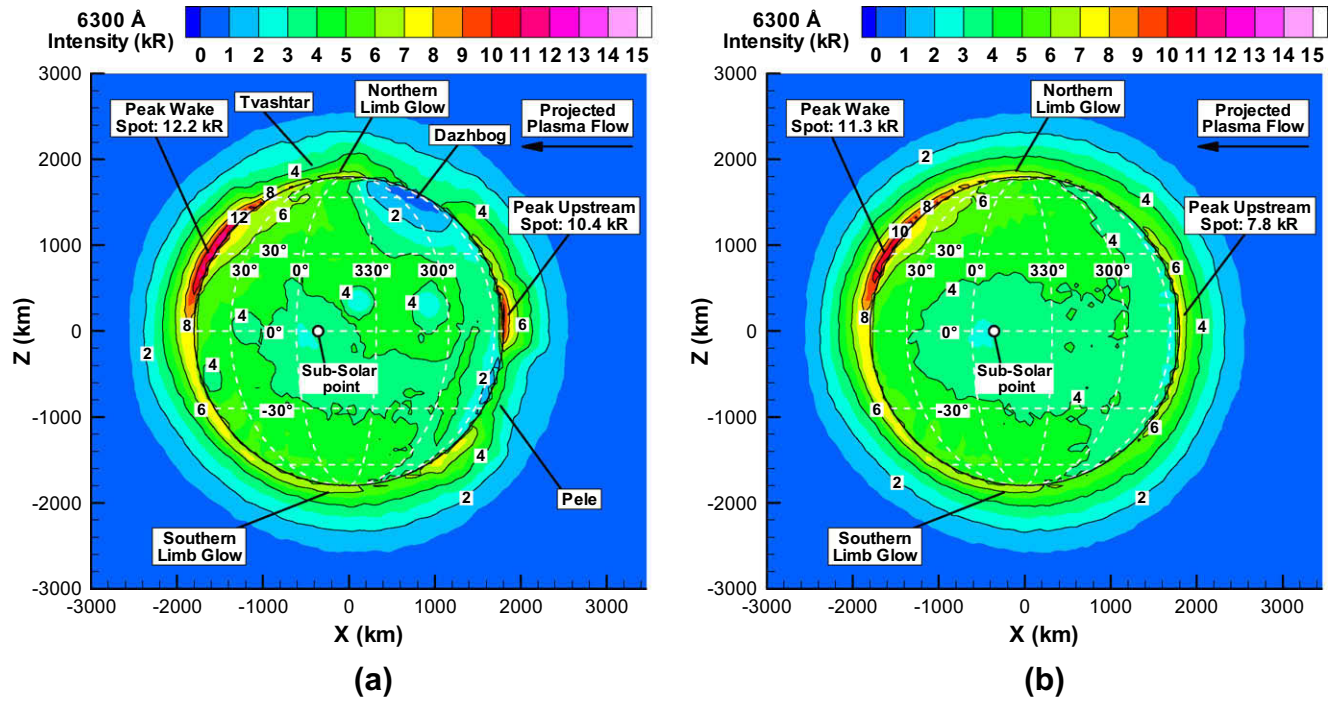


**Fig. 15.** Simulated [OI] 6300 Å emission profiles on May 22 (a) with Tvashtar and Dazhbog active in addition to the standard plumes (Table 2) and (b) with all plumes dormant. In (a) Dazhbog is seen to decrease the emission on the upstream, northern limb and Tvashtar slightly alters the limb glow emission. With all the plumes inactive (b), the peak upstream spot intensity decreases, but the average upstream emission is unchanged as the emission now extends more evenly across the limb. The change in the upstream emission is mostly due to Pele being dormant.

gen concentrations do not produce locally bright [OI] emissions due to the low oxygen content and the increased quenching inside the plume.

Clear filter images show bright plumes (particularly Pele) as seen in Radebaugh et al. (2003), Geissler et al. (2004b), Retherford et al. (2007), and Spencer et al. (2007). As a proxy for the clear filter emission morphology, Fig. 16 shows the column integrated electron energy deposition (through all electron interactions included in our model, see Table 3) from the Earth view for the case with Tvashtar and Dazhbog active (Fig. 15a). As one might expect, we find that the large volcanic plumes are very energy-absorbing; Pele, Tvashtar, and Dazhbog are easy to see in Fig. 16. Since much of the electron energy is deposited into excitation of neutrals, this suggests that non-forbidden emission (such as FUV or MUV emission) would be bright around volcanic plumes because the lifetimes for excited states of allowed transitions are much shorter than the mean time between collisions. We also see in Fig. 16 that Dazhbog “shields” Io in the region around 300°W, 45°N from energy deposition via electrons since the electrons are scattered by the dense plume instead of continuing south along the field lines which diverge around Io. If Dazhbog is dormant, this region has  $\sim 4 \text{ erg s}^{-1} \text{ cm}^{-2}$  deposited, similar to that seen downstream of Dazhbog in Fig. 16. Tvashtar exhibits a similar effect on the electron energy deposition though it is not seen because it is on the nightside.

The upstream electron temperature was varied to investigate the [OI] 6300 Å emission sensitivity to the upstream thermal electrons' temperature. Fig. 17a and b shows the simulated emission with upstream electron temperatures of (a)  $T_e = 4 \text{ eV}$  and (b)  $T_e = 6 \text{ eV}$ . Note that examining much lower temperatures is not helpful since at  $\sim 2 \text{ eV}$  the emission intensity drops off sharply as the bulk of the electrons do not have enough energy to produce [OI] upon collision with an oxygen atom. Similarly, above  $\sim 15 \text{ eV}$  the emission intensity also drops because the bulk of electrons have energies large enough that the electron excitation cross sec-

tion for [OI] has begun to fall sharply (see Fig. 4b). As seen in Fig. 17a, the overall emission decreases as the electron temperature is reduced, especially across the disk of Io. Also, the up-

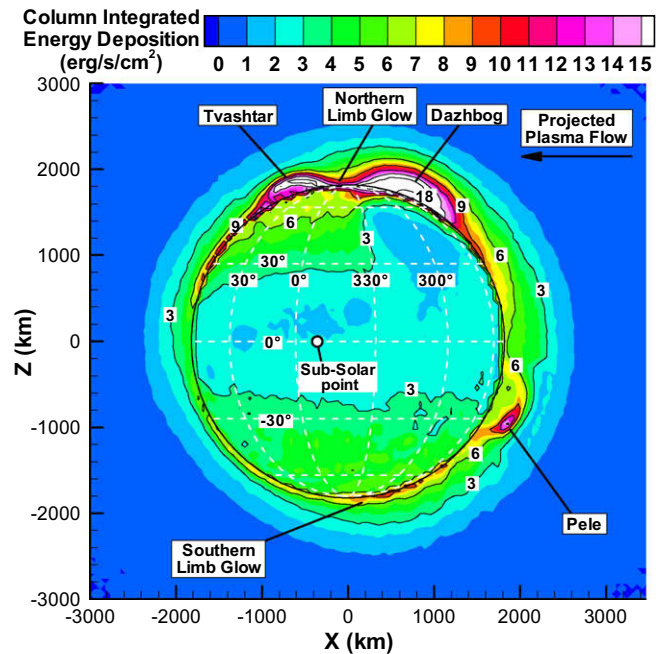


**Fig. 16.** Electron energy deposition (integrated along line of sight) into the neutral gas on May 22 by electrons with energy above 1.96 eV via the interactions listed in Table 3. We normalize the profile by the peak value. Unlike for emission profiles, absorption in the larger volcanic plumes of Pele, Tvashtar, and Dazhbog is quite apparent. This suggests that for non-forbidden emission, these plumes will be bright.

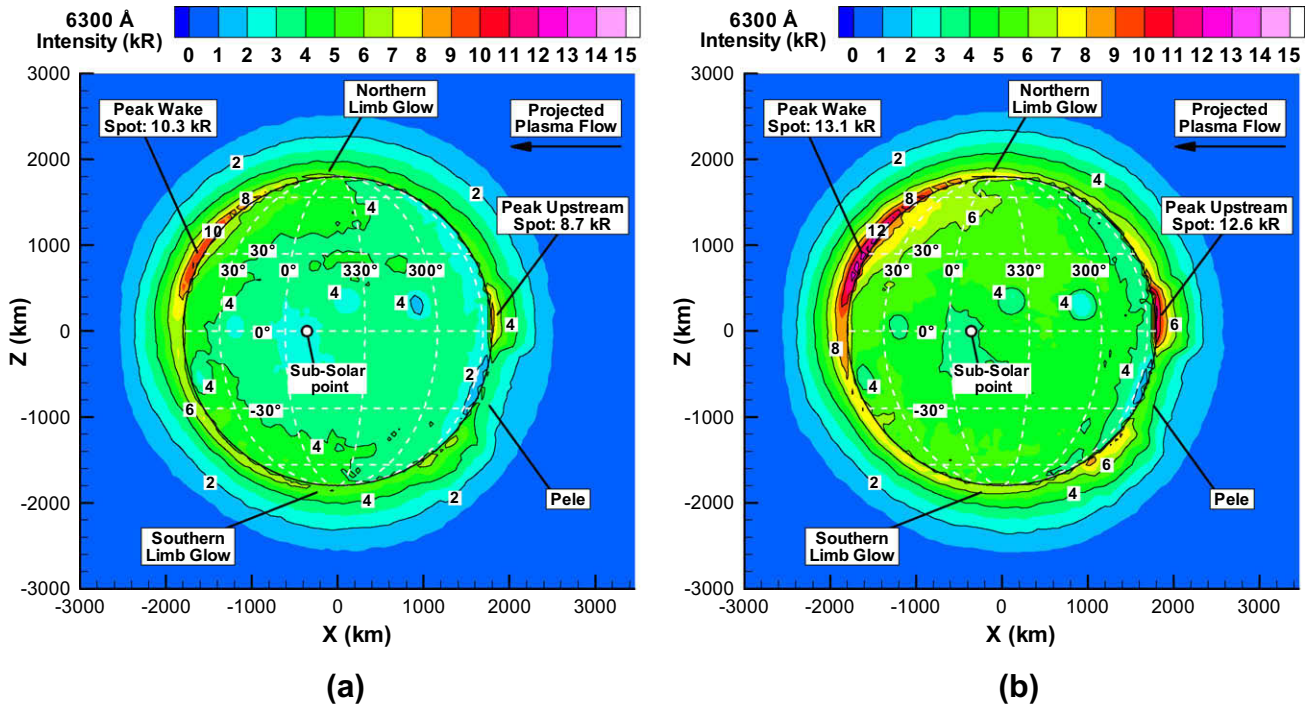


**Fig. 17.** [OI] emission on May 22 for (a) upstream electron temperature of 4 eV and (b) 6 eV. In general the emission in (a) is less intense than in (b) as might be expected because the total energy flux is higher in (b) than (a).

stream/downstream intensity ratio decreases (relative to the base case) to 0.84. Conversely, if the electron temperature increases (Fig. 17b) the overall brightness increases and the upstream/downstream brightness ratio remains the same as the base case (0.96). The vertical extent of the [OI] emission above the limb seems to be independent of the electron temperature, and is most likely controlled by the falloff of oxygen with altitude.

#### 4. Conclusions

A three-dimensional Monte Carlo (MC) model of [OI] 6300 Å emission from Io during ingress into jovian shadow was presented. The simulation accounts for the 3-D variation of SO<sub>2</sub>, O, SO, and O<sub>2</sub> in the atmosphere, several volcanic plumes, and the perturbation of the jovian magnetic field around Io. Maxwellian electrons from the jovian plasma torus with a temperature of 5 eV are input along the simulation domain boundaries and move along the magnetic field lines distorted by Io, occasionally participating in collisions with neutrals. Since the travel time for an electron flux tube to pass Io is  $\sim 520$  s and the time for individual electrons to stream along a flux tube to Io is  $\sim 190$  s, the depletion of electrons from the flux tube as it crosses Io is accounted for approximately by computing the travel time ( $T_{trip}$ ) to the torus edge and back for each electron leaving the domain, and then moving the electron downstream by  $v_{\perp,drift}T_{trip}$ .

For the base case simulation (Fig. 9b), the [OI] emission intensity in the wake is  $\sim 3$  times smaller than the observations (Fig. 6b) and the peak intensity occurs at a somewhat lower altitude, but the wake is clearly brighter than the upstream emission. Note that the observed [OI] emission intensity varies in time by up to a factor of two for Io at a given location in the torus. The discrepancy in the upstream/downstream brightness ratio most likely arises from the approximations used for the atmospheric model (e.g. use of atmosphere with  $T_{SS} = 120$  K versus  $T_{SS} = 115$  K, use of

dayside versus partially collapsed atmosphere) and the strength of the magnetic field perturbation upstream of Io. The simulated north/south limb glow feature is slightly brighter in the north than the south, though not by as much as observed.

Our simulations suggest the following:

1. *Flux tube depletion* across Io is crucial to the latitude of the wake spot. The orientation of the magnetic field itself (though the magnetic field orientation is linked to Io's location in the plasma torus) did not seem to affect the latitude of the wake spot in our simulations. However, the limitations of our magnetic field model prevent us from concluding that the field orientation has no effect on the wake spot latitude. The north/south flux tube depletion is controlled by Io's location in the torus, the divergence of the magnetic field lines around Io, the atmosphere over the poles, and the plasma drift velocity across Io.
2. *The neutral density profile* in Io's atmosphere has a significant influence on the observed aurora morphology and intensity. Our 1-D calculation shows that the dense neutral (predominately SO<sub>2</sub>) atmosphere near the surface quenches <sup>1</sup>D excited oxygen and so the near-surface region should look dark in 6300 Å emission (note that in 3-D cases, the limb is not dim because we see the total integrated column intensity). The competition between this quenching effect and the larger O density near the surface causes the emission peak to be at  $\sim 25$  km for the dayside atmosphere. In order to get the simulated peak emission to the observed altitude of  $\sim 100$  km, the vertical O profile and/or the SO<sub>2</sub> profile must change. Furthermore, weaker diffuse emission than observed was found in the simulations at high altitude ( $>400$  km). In this region, the neutral density is low enough for any <sup>1</sup>D excited oxygen to emit photons without collisional de-excitation; therefore, such diffuse or coronal emission intensity is solely a function of the vertical number density profile for oxygen at high altitudes. These results highlight the need for the use of the chemically reactive,

- 3-D DSMC atmospheric model currently under development (Walker et al., 2010); Wong and Smyth's (2000) continuum model for the atmosphere is probably not valid beyond several scale heights above the surface.
3. *The atmospheric "dayside" column* is important for matching the upstream/downstream brightness ratio since the wake spot's line of sight is partially across the dayside atmosphere. The simulation results suggest a sub-solar temperature in the vicinity of 115 K as opposed to higher temperatures (120 K). Furthermore, the partial atmospheric collapse during eclipse, and the fact that the level of collapse varies across Io, is also important for matching the upstream/downstream brightness ratio. This is because at low altitudes virtually all the  ${}^1\text{D}$  excited oxygen is collisionally quenched and therefore reducing the number density increases the emission by nearly the same proportion. Hence, even small reductions in the atmospheric density near the surface due to partial collapse can dramatically increase the overall emission.
  4. *Volcanic plumes*, especially large plumes (Pele, Tvashtar, and Dazhbog) are found to reduce the intensity of 6300 Å emission appreciably within their respective canopies. This is because of the increased probability of collisional de-excitation due to the increased neutral density. If Tvashtar (and/or Dazhbog) is active, the depletion of the electron flux tubes as they cross the northern hemisphere of Io is reduced due to increased scattering off the dense plume canopies. This impacts the overall upstream/downstream brightness ratio. Furthermore, large energy deposition into the plumes (especially Pele-sized plumes) explains why the plumes are visible in emission for optically allowed transitions. Finally, Pele and Dazhbog (if active) locally decrease the upstream intensity and in the process increase the intensity just outside of the dense canopy, noticeably altering the upstream emission morphology.
  5. *The perturbed magnetic field* in the vicinity of Io affects the emission morphology since the magnetic field is weaker in the wake and stronger upstream. Because of the magnetic mirror effect, the weaker magnetic field can trap electrons after a collision and may result in enhanced wake emission as trapped electrons have more chances to excite oxygen atoms. On the other hand, electrons with a large pitch angle ( $\sim 68^\circ$ ) are reflected by the stronger magnetic field upstream. This results in reduced upstream emission because many electrons never reach the atmosphere on the upstream side of Io.
  6. [SII] 6716 Å emission was examined through parametric study of the excitation cross section. We found that [SII] emission is much weaker than [OI] 6300 Å emission even if the cross section is unrealistically high. The reason for the lack of [SII] emission was twofold: (i) the Einstein-A coefficient for [SII] emission is  $\sim 10$  times smaller than the coefficient for [OI] emission allowing for more-frequent quenching and (ii) the density of  $\text{S}^+$  is relatively low.

## Acknowledgments

Based on observations with the NASA/ESA Hubble Space Telescope. Archival research support for Program 9535 was provided by NASA through a grant from the Space Telescope Science Institute, which is operated by the Associated Universities for Research in Astronomy, Incorporated, under NASA Contract NAS5-26555. This work was supported by STScI Grant HST-AR-10322.01-A and NASA Grants NAG5-11991 and NNX08AQ49G. The authors acknowledge the Texas Advanced Computing Center (TACC) at The University of Texas at Austin for providing HPC resources that have contributed to the research results reported within this paper.

The authors would like to thank M. Combi for use of his model magnetic field, Kurt Rutherford for helpful discussions, and the referees for constructive comments.

## References

- Acuña, M.H., Neubauer, F.M., Ness, N.F., 1981. Standing Alfvén wave current system at Io: Voyager 1 observations. *J. Geophys. Res.* 86, 8513–8521.
- Acuña, M.H., Behannon, K.W., Connerney, J.E.P., 1983. Jupiter's magnetic field and magnetosphere. In: *Physics of the Jovian Magnetosphere*. Cambridge Univ. Press, New York, pp. 1–50.
- Ajello, J.M., Hansen, D.L., Beegle, L.W., Terrell, C.A., Kanik, I., James, G.K., Makarov, O.P., 2002. Middle ultraviolet and visible spectrum of  $\text{SO}_2$  by electron impact. *J. Geophys. Res.* 107 (A7), 1099, doi:10.1029/2001JA000122.
- Austin, J.V., Goldstein, D.B., 2000. Rarefied gas model of Io's sublimation driven atmosphere. *Icarus* 148, 370–383.
- Bagenal, F., 1985. Plasma conditions inside Io's orbit – Voyager measurements. *J. Geophys. Res.* 90, 311–324.
- Bagenal, F., Sullivan, J.D., 1981. Direct plasma measurements in the Io torus and inner magnetosphere of Jupiter. *J. Geophys. Res.* 86, 8447–8466.
- Baklouti, D., Schmitt, B., Brissaud, O., 2008.  $\text{S}_2\text{O}$ , polysulfuroxide and sulfur polymer on Io's surface? *Icarus* 194, 647–659.
- Ballester, G.E., Strobel, D.F., Moos, H.W., Feldman, P., 1990. The atmosphere abundance of  $\text{SO}_2$  on Io. *Icarus* 88, 1–23.
- Ballester, G.E., McGrath, M.A., Strobel, D.F., Zhu, X., Feldman, P.D., Moos, H.W., 1994. Detection of the  $\text{SO}_2$  atmosphere on Io with the Hubble Space Telescope. *Icarus* 11, 2–17.
- Bhardwaj, A., Michael, M., 1999a. On the excitation of Io's atmosphere by the photoelectrons: Application of the analytical yield spectral model of  $\text{SO}_2$ . *Geophys. Res. Lett.* 26, 393–396.
- Bhardwaj, A., Michael, M., 1999b. Monte Carlo model for electron degradation in  $\text{SO}_2$  gas: Cross sections, yield spectra, and efficiencies. *J. Geophys. Res.* 104, 24713–24728.
- Bird, G., 1994. *Molecular Gas Dynamics and the Direct Simulation of Gas Flows*. Oxford Univ. Press, Oxford.
- Carlson, R.W., and 10 colleagues, 1997. The distribution of sulfur dioxide and other infrared absorbers on the surface of Io. *Geophys. Res. Lett.* 24, 2479–2482.
- Clark, I.D., Noxon, J.F., 1972. Optical emission from  $\text{O}({}^1\text{D})$  and  $\text{O}_2$  ( ${}^1\text{S}_g$ ) in ultraviolet photolysis of  $\text{O}_2$  and  $\text{CO}_2$ . *J. Chem. Phys.* 57, 1033–1038.
- Clarke, J., Ajello, T.J., Luhmann, J., Schneider, N., Kanik, I., 1994. HST UV spectral observations of Io passing into eclipse. *J. Geophys. Res.* 99, 8387–8402.
- Combi, M.R., Kabin, K., Gombosi, T.I., De Zeeuw, D.L., 1998. Io's plasma environment during the Galileo flyby: Global three-dimensional MHD modeling with adaptive mesh refinement. *J. Geophys. Res.* 103, 9071–9081.
- Douté, S., Schmitt, B., Lopes-Gautier, R., Carlson, R., Soderblom, L., Shirley, J., and the Galileo NIMS Team, 2001. Mapping  $\text{SO}_2$  frost on Io by the modeling of NIMS hyperspectral images. *Icarus* 149, 107–132.
- Fanale, F.P., Brown, R.H., Cruikshank, D.P., Clark, R.N., 1979. Significance of absorption features in Io's IR reflection spectrum. *Nature* 280, 761–763.
- Feaga, L.M., McGrath, M., Feldman, P.D., 2009. Io's dayside  $\text{SO}_2$  atmosphere. *Icarus* 201, 570–584.
- Frank, L.A., Paterson, W.R., Ackerson, K.L., Vasylunas, V.M., Coroniti, F.V., Bolton, S.J., 1996. Plasma observations at Io with the Galileo spacecraft. *Science* 274, 394–395.
- Geissler, P.E., Smyth, W.H., McEwen, A.S., Ip, W., Belton, M.J.S., Johnson, T.V., Ingersoll, A.P., Rages, K., Hubbard, W., Dessler, A.J., 2001. Morphology and time variability of Io's visible aurora. *J. Geophys. Res.* 106, 26137–26146.
- Geissler, P., McEwen, A., Phillips, C., Keszthelyi, L., Spencer, J., 2004a. Surface changes on Io during the Galileo mission. *Icarus* 169, 29–64.
- Geissler, P., McEwen, A., Porco, C., Strobel, D., Saur, J., Ajello, J., West, R., 2004b. Cassini observations of Io's visible aurora. *Icarus* 172, 127–140.
- Gratii, S.L., Walker, A.C., Levin, D.A., Goldstein, D.B., Varghese, P.L., Trafton, L.M., Moore, C.H., 2010. Multi-wavelength simulations of atmospheric radiation from Io with a 3-D spherical-shell backward Monte Carlo radiative transfer model. *Icarus*, doi:10.1016/j.icarus.2009.11.004.
- Gulley, R.J., Buckman, J., 1994. Elastic scattering of low energy electrons from sulphur dioxide. *J. Phys. B* 27, 1833–1843.
- Heyer, I., Biretta, J.A., 2004. Wide Field and Planetary Camera 2 Instrument Handbook ver. 9.0. Space Telescope Science Institute.
- Ingersoll, A.P., Summers, M.E., Schlipf, S.G., 1985. Supersonic meteorology of Io: Sublimation-driven flow of  $\text{SO}_2$ . *Icarus* 64, 375–390.
- Itikawa, Y., Ichimura, A., 1990. Cross sections for collisions of electrons and photons with atomic oxygen. *J. Phys. Chem. Ref. Data* 19 (3), 637–651.
- Jessup, K.L., Spencer, J.R., Ballester, G.E., Howell, R.R., Roesler, F., Vigel, M., Yelle, R., 2004. The atmospheric signature of Io's Prometheus plume and anti-jovian hemisphere: Evidence for a sublimation atmosphere. *Icarus* 169, 197–215.
- Jessup, K.L., Spencer, J.R., Yelle, R., 2007. Sulfur volcanism on Io. *Icarus* 192, 24–40.
- Joshiapura, K.N., Gangopadhyay, S., 2008. Electron collisions with sulfur compounds  $\text{SO}$ ,  $\text{SO}_2$ , and  $\text{SO}_2\text{AB}$  ( $\text{A} = \text{Cl}, \text{F}$ ): Various total cross sections. *J. Phys. B: Atom. Mol. Opt. Phys.* 41, 215205 (7pp).
- Kivelson, M.G., Khurana, K.K., Russell, C.T., Joy, S.P., Volwerk, M., Walker, R.J., Zimmer, Ch., Linker, J.A., 2001. Magnetized or unmagnetized: Ambiguity persists following Galileo's encounters with Io in 1999 and 2000. *J. Geophys. Res.* 106, 26121–26136.

- Kumar, S., 1985. The SO<sub>2</sub> atmosphere and ionosphere of Io: Ion chemistry, atmospheric escape, and models corresponding to the Pioneer 10 radio occultation measurements. *Icarus* 61, 101–123.
- Lellouch, E., 1996. Urey prize lecture. Io's atmosphere: Not yet understood. *Icarus* 124, 1–21.
- Linker, J.A., Kivelson, M.G., Walker, R.J., 1991. A three-dimensional MHD simulation of plasma flow past Io. *J. Geophys. Res.* 96, 21037–21053.
- Linker, J.A., Khurana, K.K., Kivelson, M.G., Walker, R.J., 1998. MHD simulation of Io's interaction with the plasma torus. *J. Geophys. Res.* 103, 19867–19877.
- Lipatov, A.S., Combi, M.R., 2006. Effects of kinetic processes in shaping Io's global plasma environment: A 3D hybrid model. *Icarus* 180, 412–427.
- McGrath, M.A., Belton, M.J.S., Spencer, J.R., Sartoretti, P., 2000. Spatially resolved spectroscopy of Io's Pele plume and SO<sub>2</sub> atmosphere. *Icarus* 146, 476–493.
- Michael, M., Bhardwaj, A., 2000a. Precipitation of energetic electrons in Io's atmosphere: Production of UV emissions. *Adv. Space Res.* 26, 1519–1524.
- Michael, M., Bhardwaj, A., 2000b. FUV emissions on Io: Role of Galileo-observed field-aligned energetic electrons. *Geophys. Res. Lett.* 27, 3137–3140.
- Moore, C.H., Miki, K., Goldstein, D.B., Varghese, P.L., Trafton, L., Zhang, J., 2004. Monte Carlo modeling of [OI] 630 nm auroral emission on Io. *Lunar Planet. Sci. XXXV*. Abstract #1983.
- Moore, C.H., Goldstein, D.B., Varghese, P.L., Trafton, L.M., Stewart, B., 2009. 1-D DSMC simulation of Io's atmospheric collapse and reformation during and after eclipse. *Icarus* 201, 585–597.
- Moore, C.H., Goldstein, D.B., Trafton, L.M., Varghese, P.L., 2010. Io's UV-V eclipse emission: Implications for Pele-type plumes. *Lunar Planet. Sci. XXXXI*. Abstract #2353.
- Moses, J.I., Zolotov, M.Y., Fegley, B.F., 2002. Photochemistry of a volcanically driven atmosphere on Io: Sulfur and oxygen species from a Pele-type eruption. *Icarus* 156, 76–106.
- Neubauer, F.M., 1998. The sub-Alfvénic interaction of the Galilean satellites with the jovian magnetosphere. *J. Geophys. Res.* 103, 19843–19866.
- Oliversen, R.J., Scherb, F., Smyth, W.H., Freed, M.E., Woodward Jr., R.C., Marconi, M.L., Retherford, K.D., Lupie, O.L., Morgensthaler, J.P., 2001. Sunlit Io atmospheric [OI] 6300 Å emission and the plasma torus. *J. Geophys. Res.* 106, 26183–26193.
- Pearl, J., Hanel, R., Kunde, V., Maguire, W., Fox, K., Gupta, S., Ponnampерuma, C., Raulin, F., 1979. Identification of gaseous SO<sub>2</sub> and new upper limits for other gases on Io. *Nature* 280, 755–758.
- Porco, C.C., and 23 colleagues, 2003. Cassini imaging of Jupiter's atmosphere, satellites, and rings. *Science* 299, 1541–1547.
- Radebaugh, J., Phillips, C., McEwen, A.S., Milazzo, M., Keszthelyi, L.P., 2003. Locations of hotspots on Io from Galileo SSI eclipse images. *Lunar Planet. Sci. XXXIV*. Abstract #2087.
- Ralchenko, Yu., Kramida, A.E., Reader, J., and NIST ASD Team, 2008. NIST Atomic Spectra Database (Version 3.1.5). National Institute of Standards and Technology, Gaithersburg, MD. <<http://www.physics.nist.gov/asd3/>> (19.03.09).
- Rathbun, J.A., Spencer, J.R., Davies, A.G., Howell, R.R., Wilson, L., 2002. Loki, Io: A periodic volcano. *Geophys. Res. Lett.* 29, 1443, doi:10.1029/2002GL014747.
- Retherford, K.D., 2002. PhD dissertation, Johns Hopkins University. Io's Aurora: HST/STIS Observations.
- Retherford, K.D., Moos, H.W., Strobel, D.F., Wolven, B.C., Roesler, F.L., 2000. Io's equatorial spots: Morphology of neutral UV emissions. *J. Geophys. Res.* 105, 27157–27166.
- Retherford, K.D., Moos, H.W., Strobel, D.F., 2003. Io's auroral limb glow: Hubble Space Telescope FUV observations. *J. Geophys. Res.* 108 (A8), 1333, doi:10.1029/2002JA009710.
- Retherford, K.D., Cheng, A., Weaver, H.A., Spencer, J.R., Strobel, D.F., 2007. New Horizons LORRI observations of Io's visible aurora in eclipse. In: Abstract presented at Magnetospheres of the Outer Planets, San Antonio, TX.
- Roesler, F.L., Moos, H.W., Oliversen, R.J., Woodward Jr., R.C., Retherford, K.D., Scherb, F., McGrath, M.A., Smyth, W.H., Feldman, P.D., Strobel, D.F., 1999. Far-ultraviolet imaging spectroscopy of Io's atmosphere with HST/STIS. *Science* 283, 353–357.
- Saur, J., Strobel, D.F., 2004. Relative contributions of sublimation and volcanoes to Io's atmosphere inferred from its plasma interaction during solar eclipse. *Icarus* 171, 411–420.
- Saur, J., Neubauer, F.M., Strobel, D.F., Summers, M.E., 1999. Three-dimensional plasma simulation of Io's interaction with the Io plasma torus: Asymmetric plasma flow. *J. Geophys. Res.* 104, 25105–25126.
- Saur, J., Neubauer, F.M., Strobel, D.F., Summers, M.E., 2000. Io's ultraviolet aurora: Remote sensing of Io's interaction. *Geophys. Res. Lett.* 27, 2893–2896.
- Saur, J., Neubauer, F.M., Strobel, D.F., Summers, M.E., 2002. Interpretation of Galileo's Io plasma and field observations: The J10, I24, I27 flybys, and close polar passes. *J. Geophys. Res.* 107 (A12), 1422, doi:10.1029/2001JA005067.
- Sharpee, B.D., Slanger, T.G., 2006. O(<sup>1</sup>D<sub>2</sub>–<sup>3</sup>P<sub>2,1,0</sub>) 630, 0, 636.4, and 639.2 nm forbidden emission line intensity ratios measured in the terrestrial nightglow. *J. Phys. Chem. A* 110, 6707–6710.
- Singhal, R.P., Haider, S.A., 1984. Analytical yield spectrum approach to photoelectron fluxes in the Earth's atmosphere. *J. Geophys. Res.* 89, 6847–6852.
- Sittler, E.C., Strobel, D.F., 1987. Io plasma torus electrons – Voyager 1. *J. Geophys. Res.* 92, 5741–5762.
- Smyth, W.H., Wong, M.C., 2004. Impact of electron chemistry on the structure and composition of Io's atmosphere. *Icarus* 171, 171–182.
- Smythe, W.D., Nelson, R.M., Nash, D.B., 1979. Spectral evidence for SO<sub>2</sub> frost or adsorbate on Io's surface. *Nature* 280, 766.
- Spencer, J.R., Jessup, K.L., McGrath, M.A., Ballester, G.E., Yelle, R., 2000. Discovery of S<sub>2</sub> gas in Io's Pele plume. *Science* 288, 1208–1210.
- Spencer, J.R., and 16 colleagues, 2007. Io volcanism seen by New Horizons: A major eruption of the Tvashtar volcano. *Science* 318, 240–243.
- Strobel, D.F., Wolven, B.C., 2001. The atmosphere of Io: Abundances and sources of sulfur dioxide and atomic hydrogen. *Astrophys. Space Sci.* 277, 271–287.
- Szmytkowski, C., Maciąg, K., Karwasz, G., 1996. Absolute electron-scattering total cross section measurements for noble gas atoms and diatomic molecules. *Phys. Scr.* 54, 271–280.
- Trafton, L.M., Caldwell, J.J., Barnet, C., Cunningham, C.C., 1996. The gaseous sulfur dioxide abundance over Io's leading and trailing hemispheres: HST spectra of Io's C 1B 2-X 1A 1 band of SO<sub>2</sub> near 2100 Angstrom. *Astrophys. J.* 456, 384–392.
- Trauger, J.T., Stapelfeldt, K.R., Ballester, G.E., Clarke, J.L., 1997. HST observations of [OI] emissions from Io in eclipse. AAS-DPS Abstract (1997DPS29.1802T).
- Walker, A.C., Gratiy, S.L., Goldstein, D.B., Moore, C.M., Varghese, P.L., Trafton, L.M., Levin, D.A., Stewart, B., 2010. A comprehensive numerical simulation of Io's sublimation-driven atmosphere. *Icarus*, doi:10.1016/j.icarus.2010.01.012.
- Wong, M.C., Johnson, R.E., 1996. A three-dimensional azimuthally symmetric model atmosphere for Io. *J. Geophys. Res.* 101, 23243–23254.
- Wong, M.C., Smyth, W.H., 2000. Model calculations for Io's atmosphere at Eastern and Western elongation. *Icarus* 146, 60–74.
- Zhang, J., Goldstein, D.B., Varghese, P.L., Gimelshein, N.E., Gimelshein, S.F., Levin, D.A., 2003. Simulation of gas dynamics and radiation in volcanic plumes on Io. *Icarus* 163, 182–197.
- Zhang, J., Goldstein, D.B., Varghese, P.L., Trafton, L., Moore, C., Miki, K., 2004. Numerical modeling of ionian volcanic plumes with entrained particulates. *Icarus* 172, 479–502.
- Zolotov, M.Y., Fegley Jr., B., 1998. Volcanic production of sulfur monoxide (SO) on Io. *Icarus* 132, 431–434.